

Updating of atomic data needed for ionization balance evaluations of krypton and molybdenum

M Mattioli¹, G Mazzitelli², K B Fournier³, M Finkenthal⁴ and L Carraro¹

¹ Consorzio RFX, Associazione Euratom-Enea sulla Fusione, Corso Stati Uniti 4, Padova, I-35127, Italy

² Associazione Euratom-Enea sulla Fusione, C R Frascati, CP 65-00044, Frascati Roma, Italy

³ Lawrence Livermore National Laboratory, PO Box 808, L-41 Livermore, CA 94550, USA

⁴ Plasma Spectroscopy Group, The Johns Hopkins University, Baltimore, MD 21218, USA


Received 26 May 2006, in final form 5 September 2006

Published 20 October 2006

Online at stacks.iop.org/JPhysB/39/4457

Abstract

Atomic data for both ionization and recombination of Kr and Mo ions are reviewed, the rates for these processes needing to be regularly updated following the publication of new theoretical calculations and new experimental data. Kr is used in magnetic-confinement fusion devices to produce a peripheral radiating mantle meant to spread the heat load on the plasma-facing components. In a few tokamaks Mo tiles cover the plasma-facing surfaces, acting in most cases as a plasma-column limiter. The collected atomic data represent the state of the art on the ionization and recombination data for the two considered elements. Samples of rates are proposed for both ionization and recombination along with tables of the fractional abundances at ionization equilibrium. The proposed rates should be included in codes that simulate the impurity behaviour in magnetic-confinement fusion devices, i.e., when radial transport is added to ionization and recombination to predict spatially resolved charge-state distributions to be compared with experimental results. As an example, the simulation of a Mo laser blow-off injection on the JET tokamak is re-analysed with the revised rates and multiplicative correction factors are obtained for the rate ratios recombination over ionization for L-shell ions.

 This article has associated online supplementary data files

(Some figures in this article are in colour only in the electronic version)

1. Introduction

For the interpretation of experimental data from both astrophysical sources and magnetic-confinement fusion (MCF) devices atomic data for both ionization and recombination are required. The rates for these processes have to be regularly updated following the publication

of new theoretical calculations and new experimental data. Astrophysicists usually consider only elements up to Cu ($Z = 29$) or Zn ($Z = 30$). An article that updates recommended data from recent references is published every five or six years allowing the determination of charge-state distributions (CSD) at ionization equilibrium (IE). At present, the most recent article in this context is the 1998 paper from Mazzotta *et al* [1], which has been extended in [2] from Cu to Ge ($Z = 32$). Since experimental data from both Kr ($Z = 36$) and Mo ($Z = 42$) are available from MCF devices, atomic data are also needed for these two elements. Their radiation-loss patterns were considered first by Post *et al* [3, 4] and, more recently, by Fournier *et al* [5, 6].

Inert gases (Ne, Ar, Kr) can be added in MCF devices to the fuelling gas to produce a peripheral radiating mantle that spreads the heat load on the plasma-facing components. Interest in these inert-gas scenarios has been increased by the fact that improved-confinement and high-density regimes (called radiatively improved [RI] modes) have been obtained both on limiter and divertor tokamaks such as JET, DIII-D and TEXTOR [7–10]. On the other hand, in the Alcator C-Mod and FTU devices Mo tiles cover the plasma-facing surfaces, acting in most cases as a plasma-column limiter. For Kr, May *et al* [11] obtained experimentally Kr ion density profiles and the associated cooling rates on FTU, which were tested against the model proposed by Fournier *et al* in [5]. For Mo, both on Alcator C-Mod and on FTU similar comparisons are reported in [12] with calculated radiative losses in [6]. On TEXTOR Mo accumulation has been reported both with a test Mo limiter [13] and in the presence of Ne edge radiation cooling [10]. Between the other published papers focused on the Mo ion distribution one should mention [14, 15] and [16], respectively, for Alcator C-Mod and FTU. At present an open question is the Mo ion CSD, when the central electron temperature T_e is larger than about 4 keV, i.e., when the most abundant ions range from F-like to Li-like. On FTU Pacella *et al* [17] analysed with moderate spectral resolution the 0.5–5.5 Å spectral range for a plasma heated to ~7–8 keV by electron cyclotron resonance heating. The Mo spectrum (due to $\Delta n = 1$ 3–2 transitions) could be simulated with the central plasma near coronal equilibrium and with impurity peaking. On the other hand, Mattioli *et al* [18] analysed Mo spectra from the JET tokamak in the 35–50 Å spectral range, where the Mo lines originate from $\Delta n = 0$ 2–2 transitions of F-like to Be-like ions. With the CSD data for Mo quoted in [16], it was not possible to simulate the JET Mo spectrum obtained by laser blow-off (LBO) injection. It has been necessary to modify the CSD by reducing by a factor of 2 the ionization/recombination ratio for F-like to B-like ions. On the other hand, for hot (>4 keV) FTU plasmas it has not been possible to conclude if the same correction was necessary. Finally, since theory predicts central peaking of impurities in MCF devices increasing in strength with the atomic number Z , the comparison of the behaviour of different Z elements is necessary in impurity-transport studies. Examples of such studies (i.e., when different elements are analysed in similar discharges with weak gas seeding and/or with LBO injections) have already been reported on ASDEX Upgrade and on JET [19, 20]. Mo and Kr have been considered, respectively, in [18, 19].

In our previous work on impurity transport for Kr the atomic data came, at least for the highly charged ions, from [5], whereas for Mo, as already said, the corresponding data have been described in [16]. Concerning ionization, Kr ionization-rate coefficients have been obtained recently by Loch *et al* for all the 36 ions [21], but the corresponding rate coefficients for the 42 Mo ions are not available at the moment. Experimental ionization cross sections are available for all ions up to Ar-like Kr XIX (with the exception of Zn-like Kr VII) and up to Se-like Mo IX; these cross-section data are summarized in section 2. In section 3, from fits to the cross sections as a function of energy, ionization-rate coefficients are evaluated. The difficulty caused by the presence of populated metastable levels (related to the electron density inside the source) in the ion beams extracted from the ion sources where the cross-section data

were measured is discussed. We justify the use of experimental data, where available, for the ionization rates to be used for simulating impurity behaviour in MCF devices. In the absence of these data theoretical rates are proposed.

In section 4, recombination data are assessed. For dielectronic recombination (DR) a coordinated programme has been started under the leadership of Nigel Badnell of the University of Strathclyde [22]. In this reference, goals and methodology of the modelling of finite-density plasmas are discussed. All the elements up to Zn are included, plus Kr, Mo and Xe. Tables of coefficients from fits of the detailed calculations are proposed. Not only is the T_e range of collisionally ionized plasmas considered (i.e., that of MCF devices), but calculations also extend down to the low- T_e , astrophysical photoionized plasmas. For all the sequences from recombining H-like to Na-like ions (but not yet for the He-like recombining sequence) papers have been published in *Astronomy and Astrophysics*. Everything is ‘centralized’ on the University of Strathclyde web site [23], where tables are given for all the sequences from recombining H-like to Na-like ions. On the same web site similar tables for radiative recombination (RR) are available for the same atomic species from recombining fully stripped to Na-like ions and a regular paper will appear [24]. The data from the coordinated programme on DR are taken from the web site, where all the corrections included in the errata to a few of the published papers can be found. For less-ionized ions, few detailed calculations exist. The general Burgess–Merts (BM) formula is used for DR [25, 26], when these are missing. For RR, on the other hand, only the simple, coarse approximation of recombination into a partially filled valence band and into H-like excited levels is available (see, e.g., the review article [27]). Its reliability has been checked by comparison with the data of [24]. Complete tables of fitting coefficients for both ionization and recombination data are given.

In section 5, CSDs at IE are evaluated using the present data and tables of the fractional abundances f_Z as a function of electron temperature T_e are given. The $f_Z(T_e)$ curves are compared with the corresponding ones from [5, 6]. We judge that the proposed ionization and recombination rates represent the state of the art of the available atomic data. The proposed rates should be included in the codes simulating impurity behaviour in MCF devices, i.e., when radial transport is added to ionization and recombination to predict spatially resolved CSDs to be compared with experimental results. Similarly in section 6, as an example, the simulation of a Mo laser blow-off injection on the JET tokamak [18] is re-analysed with the revised rates. The evaluated CSD in the plasma core is still too high and multiplicative correction factors are needed for the rate ratios recombination over ionization for the involved L-shell ions. Concluding remarks are given in section 7.

2. Ionization cross sections

2.1. Krypton ions

Experimental data on ionization cross sections σ as a function of the impacting-electron energy E are available for the Kr ions from neutral Kr I up to Ar-like Kr XIX, with the single exception of Zn-like Kr VII. These data are given in [28–38] and are individually treated in the following discussion. Supplementary unpublished $\sigma(E)$ data by D Gregory for Kr VIII and Kr X and by R Howald for Kr V can be found on the Oak Ridge National Laboratory (ORNL) web site [39]. Recommended data (updated in 1998 at the Queen’s University, Belfast) for Kr I–IV and theoretical $\sigma(E)$ for Kr I are given, respectively, in [40, 41].

For ion-transport simulations ionization-rate coefficients S_{ion} as functions of T_e are necessary; these rates are obtained integrating the $\sigma(E)$ curves over a Maxwell electron-

energy distribution. For an analytical integration, one must use suitable fits to the data. The four-parameter formula proposed by Younger [42] for direct ionization (DI) appeared to us to be the more suitable for smoothing the experimental curves,

$$\sigma(E) = \frac{1}{uI} [A(1 - 1/u) + B(1 - 1/u)^2 + CLn(u) + DLn(u)/u] \quad (1)$$

where $u = E/I$ is the ratio between E and the ionization potential I .

This analytical formula is based on fits of distorted-wave-exchange cross-section calculations. It provides a smooth transition between the low energy data and the asymptotic Bethe limit (C being the Bethe constant). For DI from any individual shell formula (1) requires A and C to be positive and B and D negative. Isoelectronic parameterization of the four parameters as a function of the nuclear charge Z is possible. In papers evaluating the CSD (e.g., [1, 2, 43]), the DI cross sections are obtained, according to formula (1), adding the contribution of the outer shell and of one or two inner shells. Then for each contributing shell the sign constraint is kept. Our utilization of formula (1) is different, it is just a fitting formula used for experimental ionization cross sections when both direct (from outer and inner shells) and indirect (e.g., inner-shell excitation followed by autoionization, ISEA) processes are superposed, but ISEA edges are missing. Consequently, there is no reason to keep the sign constraint.

When ISEA edges occur, the experimental curve is extrapolated above the edge in some way homothetically with theoretical DI curves and fitted with formula (1). The remaining part of the $\sigma(E)$ curve (the ISEA σ_{EA} curve) is fitted with the formula proposed for ISEA in [43]. However, since for some ions the E range of the ISEA curve is not very extended, it appeared necessary to add a sixth term with a $(1 - 1/u^4)$ dependence. Consequently, the fitting formula becomes

$$\sigma_{\text{EA}}(u) = \frac{1}{uI_{\text{EA}}} [A + B(1 - 1/u) + C(1 - 1/u^2) + D(1 - 1/u^3) + E(1 - 1/u^4) + FLn(u)] \quad (2)$$

where now $u = E/I_{\text{EA}}$ is the ratio between E and the ISEA ionization threshold I_{EA} taken at the ‘bump’ edge. The procedure followed is shown in figure 1, where, for Kr XVI–XIX (Sc-like to Ar-like ions) from [38], the blue stars show the experimental cross sections, the red broken curve the extrapolated ‘DI’ cross sections, the magenta stars the expanded ‘ISEA’ cross sections fitted by the full magenta curves. The ISEA ‘bumps’ (caused by inner-shell excitation of 2s and 2p levels), are real, since they are well above the range of the quoted uncertainties on $\sigma(E)$, typically $2\text{--}3 \times 10^{-20} \text{ cm}^2$. For the other, less-ionized ions considered in [38] possible ISEA ‘bumps’ are below the reported uncertainties and are consequently neglected.

In figures 2–4, the black full curves show the chosen fits of the available experimental data for $\sigma(E)$ ($\sigma(E) + \sigma_{\text{EA}}(E)$ for Kr XVI–XIX). The colour curves show the various data available that were used for the fits, the references from which they were taken are given in the captions. When there are differences between the data (e.g., Kr I–V), lacking any preference criterion, the black curves represent the average of the individual fits. We must remark that the differences between the various curves for the same ion can be outside the error bars of the individual measurements. For Kr I (figure 2), the theoretical blue chain curve [41], with a larger maximum value, has not been considered. Moreover, it must be observed that, with the single exception of neutral Kr, the complete ionization calculations reported in [21] can be considered always in good or fair agreement with either the experimental data or with other theoretical calculations (e.g., [44, 45]).

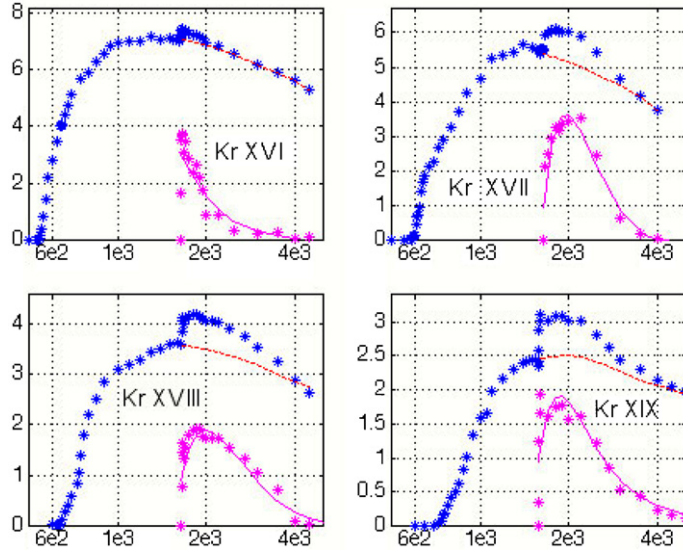


Figure 1. (From left to right and from top to bottom, units $1 \times 10^{-19} \text{ cm}^2$ and eV.) Blue full curve: experimental ionization cross sections $\sigma(E)$ for Kr XVI–XIX; red broken curve: DI cross section σ_{DI} extrapolated above the ISEA edge; magenta: expanded ISEA cross section $\sigma_{\text{EA}}(E)$, stars experimental points and full curves fits according to formula (2) (Kr XVI *10, Kr XVII *4, Kr XVIII–XIX *3).

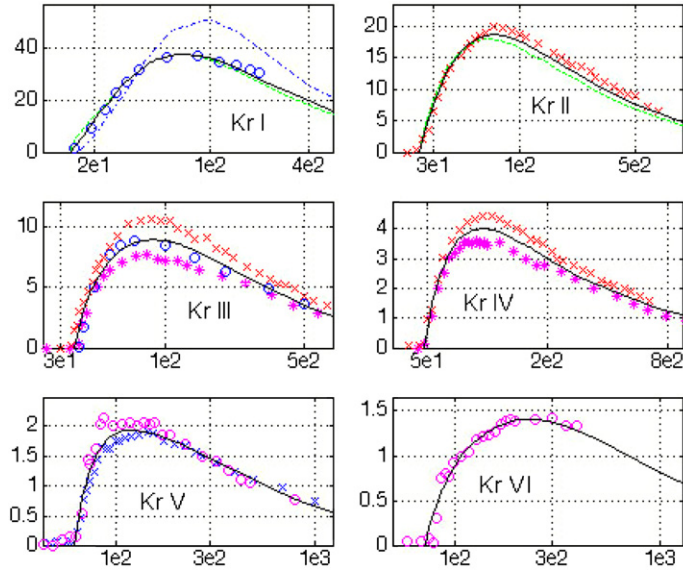


Figure 2. (From left to right and from top to bottom, units $1 \times 10^{-17} \text{ cm}^2$ and eV.) Experimental ionization cross sections $\sigma(E)$ for Kr I–VI; black thick full curves: selected fits according to formula (1); Kr I: blue circles [29], green full [40], blue chain (not considered for the fit) [41], not shown [28] almost coincident with black curve; Kr II: red crosses [32], green broken [40] = [30]; Kr III: red crosses [32], blue squares [31], magenta stars [33] = [40]; Kr IV: red crosses [32], magenta stars [34] = [40]; Kr V: magenta circles [35], blue crosses [39]; Kr VI: magenta circles [35].

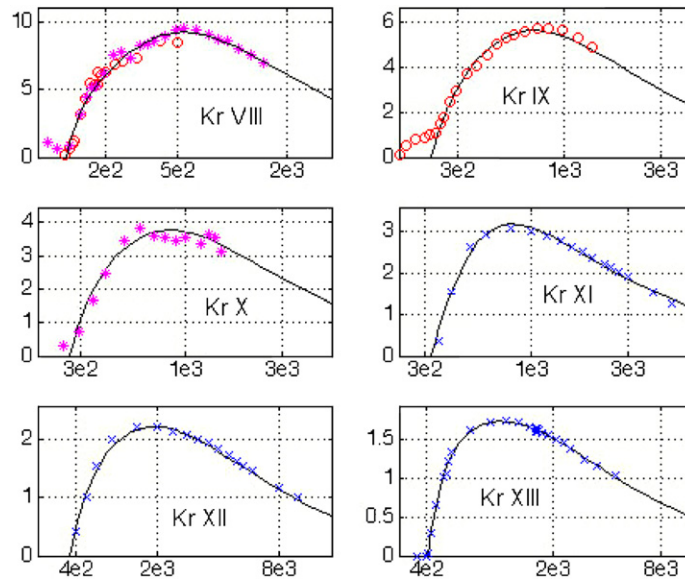


Figure 3. (From left to right and from top to bottom, units $1 \times 10^{-18} \text{ cm}^2$ and eV.) Experimental ionization cross sections $\sigma(E)$ for Kr VIII–XIII; black full curves: selected fits according to formula (1); Kr VIII: red circles [35], magenta stars [39]; Kr IX: red circles [36]; Kr X: magenta stars [39]; Kr XI–XII: blue crosses [37]; Kr XIII: blue crosses [38].

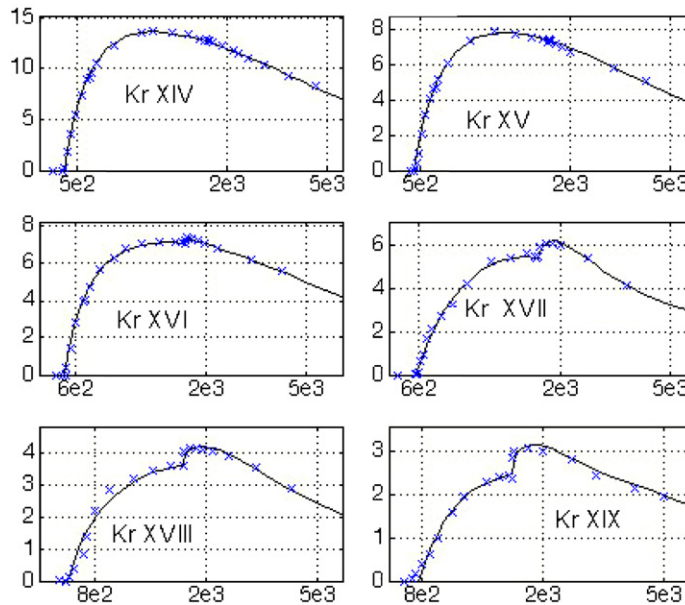


Figure 4. (From left to right and from top to bottom, units $1 \times 10^{-19} \text{ cm}^2$ and eV.) Experimental ionization cross sections $\sigma(E)$ for Kr XIV–XIX; black full curves: selected fits according to formula (1), including contribution of ISEA according to formula (2) for Kr XVI–XIX; Kr XIV–XIX: blue crosses [38].

Table 1. Fit parameters A, B, C, D (units: $1 \times 10^{-14} \text{ cm}^2 \text{ eV}^2$) for evaluating DI ionization cross sections and rates according to, respectively, formulae (1) and (3). Z spectroscopic notation and I (eV) ionization potentials.

Kr ions					
Z	I	A	B	C	D
1	14	−35.3	−13.4	47	−6.5
2	24.6	−49.5	26.4	37.8	36.9
3	35	241.2	−96.7	−16.7	−183.5
4	48	28.9	−23.3	14.8	−1.0
5	62	163.8	−89.7	−4.7	−119.2
6	72	96	−56.6	13.5	−86.7
8	120	104.3	−119.0	62.8	−130.4
9	220	577.4	−253.8	−8.9	−494.6
10	265	410.6	−191.8	19.2	−356
11	320	−272.2	167.1	103.4	245.6
12	370	670.6	−263.3	−44.6	−521.7
13	405	548.8	−309.1	15.7	−439.1
14	445	472.8	−291	25.4	−368.3
15	475	313.2	−174.8	7.8	−239.9
16	540	260.2	−203.7	53.2	−217.6
17	585	226.9	−69.7	−3.8	−166.4
18	640	501.1	−202.6	−49.3	−398.3
19	780	205.7	−109.0	13.7	−158.5

Table 2. Fit parameters A, B, C, D, E, F (units: $1 \times 10^{-16} \text{ cm}^2 \text{ eV}$) for evaluating ISEA ionization cross sections and rates according to, respectively, formulae (2) and (6). Z spectroscopic notation and IEA (eV) ISEA edges.

Kr ions							
Z	IEA	A	B	C	D	E	F
16	1640	0.5	−1.7	0	0	0	0.6
17	1650	0.4	45.9	−82.6	45.7	0	−1.5
18	1650	0.5	3.5	−17.5	12.9	0	0.4
19	1580	0.5	−0.1	7.6	−22.6	15.4	−0.3

The four fit parameters for DI (in units $10^{-14} \text{ cm}^2 \text{ eV}^2$) are given in table 1, along with the ionization potentials I (in eV). On the other hand, the six fit parameters for ISEA (in units $10^{-16} \text{ cm}^2 \text{ eV}$) are given in table 2, along with the ISEA ionization potentials I_{EA} (in eV) taken at the edge or, rather, at the discontinuity of $\sigma(E)$.

The values of DI ionization potential I are chosen empirically before the fits and are determined for each ion in such a way that the fitted curve, starting at $u = 1$, follows well the increase of the experimental data. The given I -values can be smaller than the ground state ionization potentials I_{g} found in the literature, due to the presence of the beams extracted from ion sources of populated metastable levels with lower ionization potentials. As a consequence of the choice of I , the small features caused by metastable levels in the threshold region are excluded from the fits (the clearest example being Kr IX in figure 3). When $I < I_{\text{g}}$, it is not possible to give a general assessment that quantifies how much contribution to the total measured cross section comes from levels other than the ground level. Each ion constitutes a particular case and is treated in the original reference when discussing the experimental data.

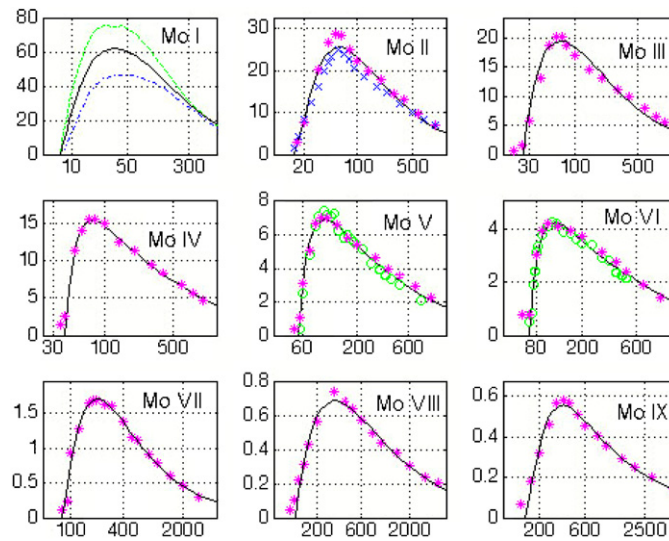


Figure 5. (From left to right and from top to bottom, units $1 \times 10^{-17} \text{ cm}^2$ and eV.) Experimental ionization cross sections $\sigma(E)$ for Mo I–IX; black full curves: selected fits according to formula (1); Mo I: green broken [40], blue chain [41]; Mo II: blue crosses [48] = [40], magenta stars [49]; Mo III–IV: magenta stars [49]; Mo V–VI: green circles [50], magenta stars [49]; Mo VII–IX: magenta stars [49].

The metastable-level population is related to the electron density n_e in the ion source; levels above the ground state are populated (and de-populated) through electron collisions. Unfortunately, the electron density in these sources is highly uncertain and device dependent; it is guessed to be in the 10^{11} – 10^{12} cm^{-3} range rather than directly measured. In MCF devices typical n_e -values are roughly two orders of magnitude higher, and metastable levels are populated, as confirmed by both experimental observations and atomic physics modelling. For example, in the Be-like isosequence for O the lowest singlet and triplet levels have comparable populations (the singlet and triplet, 630 and 760 Å, lines being of comparable brightnesses). On the other hand, for Kr and Mo the corresponding triplet lines are much weaker than the resonance line, since the metastable population decreases with the atomic number and increases with the electron density.

Since our calculations are planned for impurity simulations in MCF devices, we always propose to use the experimental data when available. Our decision is supported by the fact that Pindzola *et al* [46, 47], in their corresponding reviews of Fe and Ni ionization data, also recommend the experimental data, even if a clear contribution of metastable levels is present.

On the other hand, for astrophysicists the contributions of metastable levels to the experimental data are a serious problem since, generally, the n_e -values with which they are involved are much lower than those in the ion sources. If the metastable contribution cannot be subtracted, astrophysical modellers tend to prefer theoretical data.

2.2. Molybdenum ions

For molybdenum, experimental $\sigma(E)$ are available for Mo II–IX [48–50], whereas for neutral Mo two theoretical calculations have been found in [40, 41]. Data for these nine ions have been fit according to formula (1). We must underline that for simplicity we have considered implicitly in the text neutral Mo as having experimental data. In figure 5 the black full curves

Table 3. Fit parameters A, B, C, D (units: $1 \times 10^{-14} \text{ cm}^2 \text{ eV}^2$) for evaluating DI ionization cross sections and rates according to, respectively, formulae (1) and (3). Z spectroscopic notation and I (eV) ionization potentials.

Mo ions					
Z	I	A	B	C	D
1	7.1	-89.3	21	34	59.1
2	13.6	-70.0	30.9	29.2	39.5
3	26	0.3	-5.2	36.8	2.7
4	40	35.7	-118.6	84.2	7.6
5	54	165.9	-137.5	32.1	-88.9
6	68.5	315.8	-236.9	20.5	-213.3
7	80	-60.7	57.4	22.5	61.4
8	115	-24.4	12.1	27.8	20.7
9	140	-253.9	140.5	53.7	217.8
42	24600	-50.42	13.14	17.92	36.96

show the chosen fits for $\sigma(E)$. As with Kr, the colour curves show the various data available used for the fits, the references from which they were taken are given in the captions. No ISEA ‘bump’ is evident for these ions, in spite of the fact that both direct and indirect processes can contribute to their $\sigma(E)$. The four fit parameters for DI are given in table 3, along with the ionization potentials I , obtained as previously explained for Kr.

3. Ionization-rate coefficients

3.1. Krypton ions

For all the ionization cross sections fitted above, the direct ionization-rate coefficients $S_{\text{ion}}(T_e)$ (in units of cm^3/s) are obtained as function of T_e according to the following formula:

$$S_{\text{ion}} = 6.69 \times 10^7 \frac{\exp(-x)}{T_e^{3/2}} F(x) \quad (3)$$

where $x = I/T_e$ (both in eV) and

$$F(x) = A[1 - xf_1(x)] + B[1 + x - x(2 + x)f_1(x)] + Cf_1(x) + Dx f_2(x) \quad (4)$$

with the four fitting parameters in units $10^{-14} \text{ cm}^2 \text{ eV}^2$ and the functions $f_1(x)$ and $f_2(x)$ given by

$$f_1(x) = e^x \int_1^\infty \frac{dt}{t} e^{-tx} \quad f_2(x) = e^x \int_1^\infty \frac{dt}{t} e^{-tx} \text{Ln}(t). \quad (5)$$

Analytical approximations are available for both $f_1(x) = e^x \text{expint}(x)$ and $f_2(x)$.

For ISEA the ionization rate (in units of $\text{cm}^3 \text{ s}^{-1}$) is

$$S_{\text{ISEA}} = 6.69 \times 10^7 \frac{\exp(-x)}{T_e^{1/2}} F_2(x) \quad (6)$$

where now $x = I_{\text{EA}}/T_e$ (both in eV) and $F_2(x)$ is given by

$$F_2(x) = A + B[1 - xf_1(x)] + C[1 - x(1 - xf_1(x))] + D[1 - 0.5(x - x^2 + x^3 f_1(x))] + E[1 - (x - x^2/2 + x^3/2)/3 + x^4 f_1(x)/6] + F f_1(x) \quad (7)$$

with the six fitting parameters in units of $10^{-16} \text{ cm}^2 \text{ eV}$.

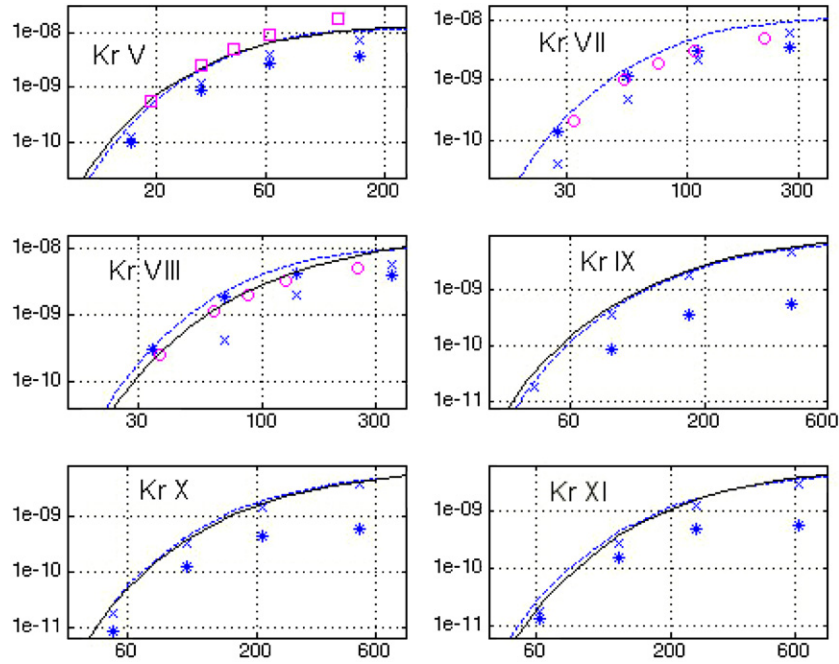


Figure 6. (From left to right and from top to bottom, units $\text{cm}^3 \text{s}^{-1}$ and eV.) Ionization-rate coefficients $S_{\text{ion}}(T_e)$ for Kr V and Kr VII–XI; black full curves: selected fits according to formula (3), except for Kr VII; blue: rates from [21] (broken curves interpolated total rates, crosses DI, stars ISEA with unit autoionization branching ratio); magenta: squares Kr V total [51], circles Kr VII–VIII ISEA [52, 53].

Since Loch *et al* [21] presented tables of S_{ion} for all 36 Kr ions, interpolated values from that work have been taken as reference for comparison with rate coefficients obtained from integrating the experimental cross-section data over a Maxwellian electron-energy distribution. For several ions up to Ar-like Kr XIX in figures 6 and 7, the black full curves are obtained using formula (3) (including the contribution of ISEA according to formula (6) for Kr XVI–XIX), whereas the blue broken ones are the interpolated total-ionization rates from [21] (the crosses and the stars showing, respectively, the DI and ISEA contributions in the tabulated data). Four ions (Kr II–IV and Kr VI) with practically superposed full and broken curves are not shown, whereas for neutral Kr, as already mentioned when discussing the ionization cross sections, the theoretical rate coefficients are two times larger than the experimental ones. In figure 6, for comparison, (magenta squares) the S_{ion} -values from Mandelbaum *et al* for Ge-like Kr V [51] and (magenta circles) the S_{ISEA} -values from Mitnik *et al* [52, 53] for Zn-like Kr VII and Cu-like Kr VIII are also plotted.

In [5], DI ionization-rate coefficients for Kr XXIV–XXXVI (Al-like to H-like ions) and ISEA rate coefficients for Kr XXI–XXVI (S-like to Na-like ions) can be found. For ISEA there is good agreement with [21] for Kr XXI–XXIII. In figure 8, the various rate coefficients are compared for Kr XXIV–XXVI (blue curves from [21] and red curves from [5], with more details in the captions). Differences (increasing in the keV range) are evident for Mg-like and Na-like, particularly for ISEA.

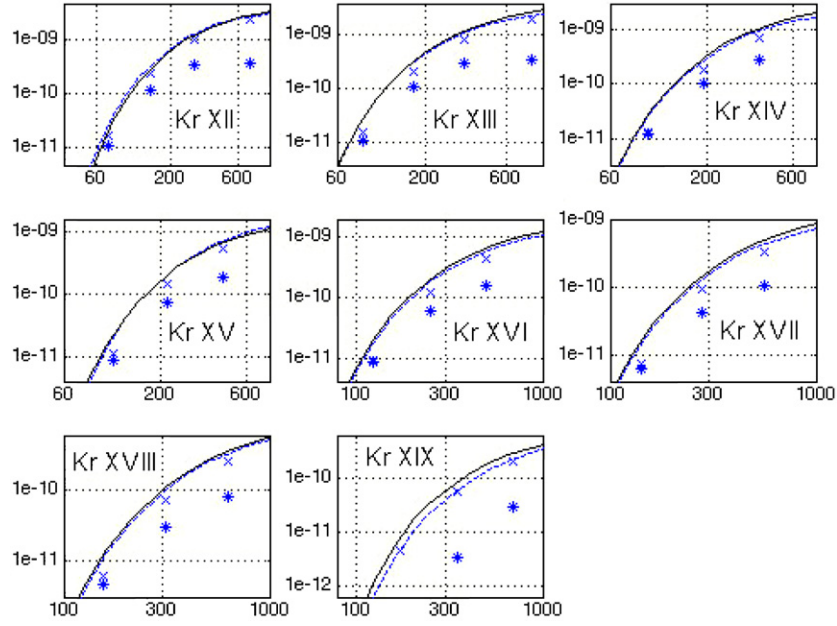


Figure 7. (From left to right and from top to bottom, units $\text{cm}^3 \text{s}^{-1}$ and eV.) Ionization-rate coefficients $S_{\text{ion}}(T_e)$ for Kr XII–XIX; black: selected fits according to formula (3), including contribution of ISEA according to formula (6) for Kr XVI–XIX; blue: rates from [21] (broken curves interpolated total rates, crosses DI, stars ISEA with unit autoionization branching ratio).

For Kr XXVII–XXXVI (Ne-like to H-like ions), a third calculation is considered with S_{ionL} (in units of $\text{cm}^3 \text{s}^{-1}$) from the well-known Lotz’s reference formula [54]

$$S_{\text{ionL}} = 6.69 \times 10^7 (aq/T_e^{3/2}) (\text{expint}(x)/x) \quad (8)$$

where $a = 4.5 \times 10^{-14} \text{ cm}^2 \text{ eV}^2$, q is the number of equivalent, peripheral electrons with ionization potential I (given in table 4, taken from Kelly’s compendium [55]), $x = I/T_e$ (both in eV) and a second term added to include the ionization of the two, inner 2s electrons for Ne-like to B-like ions. However, lacking the corresponding inner-shell ionization potentials, they are taken as approximately equal to the peripheral I -value for Be-like ions (i.e., when the inner electron becomes peripheral). It is a known overestimate, decreasing with decreasing number of peripheral electrons, when the relative inner-electron contribution is increasing. Figure 9 shows that formula (8) could be used for the same isosequences of Mo ions.

When experimental data are available (i.e., from Kr I up to Kr XIX with the exception of Zn-like Kr VII), formula (3) is used with fit parameters from table 1, along with formula (6) with fit parameters from table 2 for the ISEA contribution. For the remaining ions, we suggest using S_{ion} rates from [21] fitted (in units of $\text{cm}^3 \text{s}^{-1}$) with the following formula:

$$S_{\text{ionf}} = (10^{-11}/T_e^{1/2}) \sum_i C_i \exp(-E_i/T_e) \quad (9)$$

where the fit parameters are given in table 5 and T_e is in eV. It is the sum of terms of the kind used previously to Lotz’s formula (see, e.g., [56]). The number of parameters C_i and E_i needed for a good fit depends on the T_e range of interest; we consider the range where the fractional abundances $f_Z(T_e)$ at IE are larger than 10^{-4} – 10^{-3} .

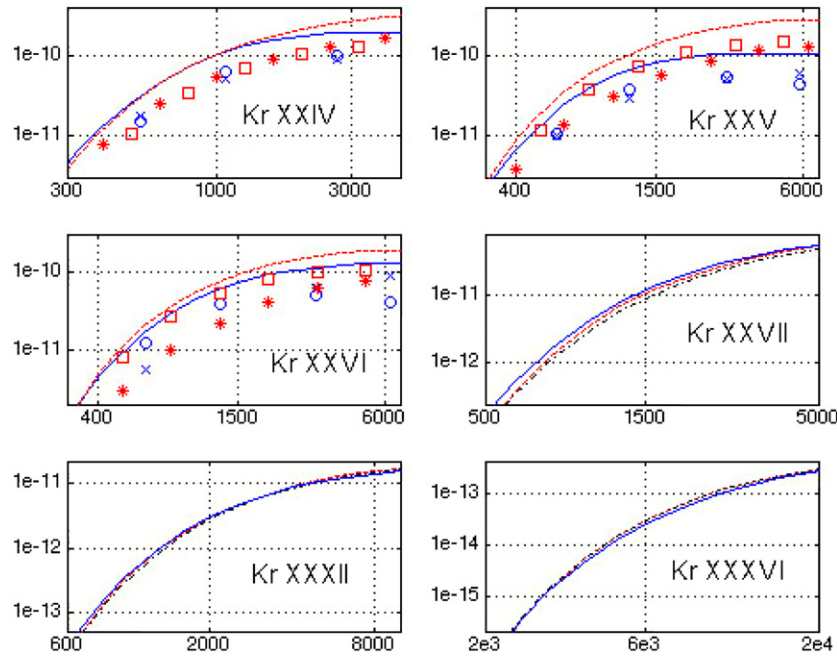


Figure 8. (From left to right and from top to bottom, units $\text{cm}^3 \text{s}^{-1}$ and eV.) Ionization-rate coefficients $S_{\text{ion}}(T_e)$ for Kr XXIV–XXVII, Kr XXXII, Kr XXXVI; blue: rates from [21] (full curves interpolated total rates, crosses DI, circles ISEA with autoionization branching ratio different from one); red: rates from [5] (broken total, stars DI, squares ISEA); black: rates from Lotz’s formula (8) for the three more ionized ions.

Table 4. Ionization potentials for highly ionized Kr and Mo ions (eV).

Isosequences	Kr ions	Mo ions
Ne-like	2953	3990
F-like	3056	4191
O-like	3203	4392
N-like	3381	4593
C-like	3555	4902
B-like	3712	5110
Be-like	3912	5407
Li-like	4105	5585
He-like	17 292	23 120
H-like	17 931	24 600

3.2. Molybdenum ions

Mo ions are treated in the same way as explained previously for the Kr ions. For Mo I–IX, the rate coefficients S_{ion} are evaluated following formula (3) with the fit parameters in table 3 and three of them (Mo VII–IX) are shown in figure 9 (black full curves). Ionization-rate coefficients for Mo VII–XIV (Kr-like to Cu-like) have been calculated by Mitnik *et al* [52, 53, 57, 58] and fitted with formula (9) with fit coefficients given in table 6. A few of these

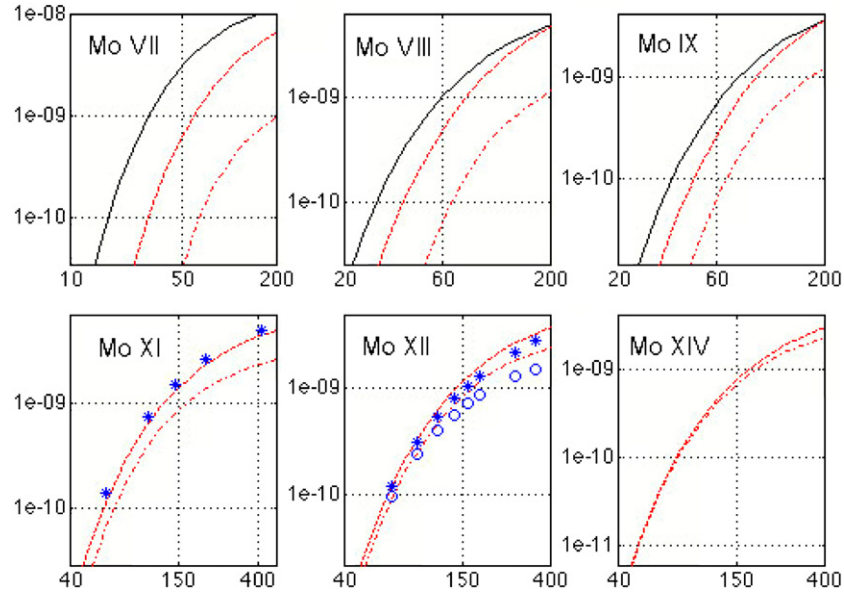


Figure 9. (From left to right and from top to bottom, units $\text{cm}^3 \text{s}^{-1}$ and eV.) Ionization-rate coefficients $S_{\text{ion}}(T_e)$ for Mo VII–IX, XI–XII, XIV; black full curves: selected fits according to formula (3), for Mo VII–IX; red: rates following Mitnik *et al* [52, 53, 57, 58] (broken total, chain ISEA); blue: stars total Mo XI [51] and Mo XII [59], circles Mo XII ISEA [59].

coefficients are shown in figure 9 (red, broken and chain curves, respectively, for total and ISEA rates). It appears clearly that for these ions the ratio DI/ISEA increases with the number of peripheral $n = 4$ electrons. Supplementary calculations for Mo XI–XII [51, 59] are also included in figure 9 (blue, stars and circles, respectively, for total and ISEA rates). The black curves from experiments, particularly for Mo VII, are above the theoretical red ones. It is not possible, at present, to say if the discrepancy is due to the presence of populated metastable levels in the ion sources or to inadequacy of the theory.

DI data are available from [6] according to formula (9) for Mo XV–XXXIII (Ni-like to Ne-like), but ISEA is available only for Mo XXIV–XXXII (K-like to Na-like ions) [60]. Table 7 lists the coefficients, where the first pair of numbers is for DI and the second for ISEA. When ISEA is missing, the comparison between DI and ISEA contributions for the Kr ions of the same isosequences, i.e. Kr IX–XVII (see figures 6 and 7) indicates that DI is always the dominating process. Consequently, while waiting for future calculations, we think that we are justified for Mo transport simulation to neglect ISEA for Mo XV–XXIII (Ni-like to Ca-like). For Mo XXXIV–XLI formula (8) is used with I -values from [61], which are also given in table 4. For H-like Mo XLII experimental cross sections are reported in [62, 63] in the 30–100 keV range. In this range they are larger than predicted by the Lotz’s formula, but they agree with the cross section evaluated by Shi *et al* [64], which studied the ionization of the H-like sequence up to Mo. Their cross sections have been fitted with formula (1) (the parameters for Mo are also given in table 3). It is observed that the two cross sections agree below 40 keV. Since in the hottest MCF devices at present the central electron temperature is, at maximum, around 10 keV, both formulae give similar values for S_{ion} in the T_e range of interest.

Table 5. *C* and *E* coefficients for evaluating ionization rates of Kr I–XXXVI according to formula (9), fits of the tabulated data of [21].

Kr ions					
<i>Z</i>	<i>C</i> 1	<i>C</i> 2	<i>C</i> 3	<i>C</i> 4	<i>C</i> 5
1	1.406×10^4	1.417×10^5	2.091×10^5	3.762×10^5	-1.247×10^5
2	1.546×10^4	3.281×10^4	1.002×10^5	1.075×10^5	
3	1.868×10^4	5.099×10^4	4.966×10^4		
4	1.306×10^4	2.714×10^4	2.372×10^4		
5	7.316×10^3	1.883×10^4	1.234×10^4		
6	5.979×10^3	2.458×10^4	-9.476×10^3	3.238×10^4	5.834×10^4
7	8.811×10^3	2.377×10^4	5.288×10^4	-1.707×10^3	
8	9.250×10^3	2.346×10^4	5.640×10^4		
9	5.847×10^3	2.109×10^4	1.301×10^4	3.524×10^4	
10	5.967×10^3	1.709×10^4	2.932×10^4		
11	5.644×10^3	1.432×10^4	2.433×10^4		
12	4.571×10^3	1.180×10^4	1.886×10^4		
13	3.941×10^3	9.655×10^3	1.492×10^4		
14	3.570×10^3	7.958×10^3	1.142×10^4		
15	2.663×10^3	6.650×10^3	9.209×10^3		
16	2.201×10^3	5.708×10^3	7.076×10^3		
17	1.649×10^3	4.844×10^3	5.704×10^3		
18	1.279×10^3	4.318×10^3	4.477×10^3		
19	9.871×10^2	3.710×10^3	3.095×10^3		
20	8.580×10^2	3.288×10^3	2.444×10^3		
21	6.411×10^2	2.496×10^3	1.241×10^3		
22	5.811×10^2	2.462×10^3	1.619×10^3		
23	4.583×10^2	2.210×10^3			
24	3.531×10^2	1.710×10^3			
25	2.294×10^2	9.118×10^2			
26	2.780×10^2	9.747×10^2	1.294×10^3		
27	1.585×10^2	4.708×10^2	8.353×10^2		
28	1.322×10^2	4.041×10^2	6.813×10^2		
29	1.089×10^2	3.269×10^2	5.477×10^2		
30	8.753×10^1	2.642×10^2	4.246×10^2		
31	6.575×10^1	1.798×10^2	3.514×10^2		
32	4.870×10^1	1.357×10^2	2.219×10^2		
33	2.971×10^1	1.013×10^2	1.629×10^2		
34	1.509×10^1	4.924×10^1	1.209×10^2		
35	2.086×10^0	1.146×10^1	3.672×10^1		
36	1.367×10^0	9.615×10^0	3.939×10^1		
<i>Z</i>	<i>E</i> 1	<i>E</i> 2	<i>E</i> 3	<i>E</i> 4	<i>E</i> 5
1	15.58	22.95	50.83	830.27	610.63
2	26.55	33.61	66.02	343.63	
3	41.07	72.86	549.98		
4	54.51	94.83	644.3		
5	69.87	118.57	868.54		
6	87.51	158.67	246.07	427.93	2077.08
7	126.49	237.26	1424.3	416.58	
8	136.37	262.98	1702.96		
9	260.14	445.85	1266.07	2878.08	
10	301.07	517.88	2012.08		

Table 5. (Continued.)

Z	Kr ions				
	E1	E2	E3	E4	E5
11	341.36	591.72	2717.66		
12	389.64	678.71	3113.23		
13	438.03	766.41	3450.5		
14	483.68	875.78	4003.39		
15	537.92	965.62	4332.71		
16	589.93	1096.03	4887.2		
17	648.72	1210.93	5506.1		
18	712.87	1381.41	6719.05		
19	883.88	1663.24	7974.53		
20	947.85	1797.41	9802.75		
21	1000.5	1749.15	4742.56		
22	1076.4	1953.53	12 336.39		
23	1142.83	2036.01			
24	1226.66	2022.62			
25	1322.52	2069.08			
26	1490.83	2474.87	12 643.79		
27	3151.5	4376.41	10 683.44		
28	3307.08	4642.69	11 589.77		
29	3480.12	4893.65	12 244.3		
30	3651.37	5192.76	13 260.98		
31	3835.22	5301.31	13 917		
32	4037.05	5829.1	14 757.38		
33	4247.48	6543.01	22 430.62		
34	4417.73	6797.18	25 679.19		
35	17 811.5	21 181.29	45 508.69		
36	18 562.84	24 656.75	113 860.55		

4. Recombination rate coefficients

4.1. Radiative recombination

As already discussed in the introduction, for recombining Na-like to fully stripped Kr and Mo ions, fitting parameters (A , b , T_0 and T_1) of the Verner-Ferland's formula [65] are available on the University of Strathclyde web site [23]. The recombination rate coefficient α_r (in units of $\text{cm}^3 \text{s}^{-1}$), with T_e in eV, is given by

$$\alpha_r = A \left[\sqrt{\frac{T_e}{T_0}} \left(1 + \sqrt{\frac{T_e}{T_0}} \right)^{1-b} \left(1 + \sqrt{\frac{T_e}{T_1}} \right)^{1+b} \right]^{-1}. \quad (10)$$

The four parameters required for equation (10), as found on the University of Strathclyde web site (updated fits C-20051227), are given in tables 8(a) and (b), respectively, for Kr and Mo. Tabulated coefficients for the ground levels are given [24].

For less ionized ions, lacking specific calculations, only a crude approximation is available: recombination processes have been treated separately for recombination into the non-hydrogenic partially filled valence shell and recombination into excited H-like shells (see, e.g., the review article by De Michelis and Mattioli [27]).

Table 6. *C* and *E* coefficients for evaluating ionization rates of Mo VII–XIV according to formula (9), using theoretical data from [52, 53, 57, 58].

Mo ions				
<i>Z</i>	<i>C</i> 1	<i>C</i> 2	<i>C</i> 3	<i>C</i> 4
7	7.938×10^3	2.851×10^4	4.671×10^4	
8	5.865×10^3	2.457×10^4	4.140×10^4	
9	4.544×10^3	2.085×10^4	3.544×10^4	
10	3.928×10^3	1.795×10^4	3.069×10^4	
11	4.173×10^3	1.574×10^4	2.699×10^4	
12	4.90×10^3	1.43×10^4	2.40×10^4	
13	9.140×10^2	1.268×10^4	1.860×10^4	2.903×10^4
14	1.947×10^3	1.034×10^4	1.720×10^4	1.630×10^4
<i>Z</i>	<i>E</i> 1	<i>E</i> 2	<i>E</i> 3	<i>E</i> 4
7	153.57	320.69	1158.93	
8	177.5	349.21	1259.32	
9	201.29	368.06	1290.63	
10	227.97	387.75	1320.88	
11	256.93	413.14	1374.29	
12	283.16	447.68	1476.27	
13	260.8	370.34	909.19	3727.01
14	302.48	411.73	1041.98	4118.62

In figure 10, the Strathclyde rates are plotted (blue full curves) for six recombining Kr ions and compared with the approximated rates (red broken curves). For the other six recombining Kr ions and for the corresponding Mo ions the discrepancies are similar, the maximum differences being for the recombining Na-like and Ne-like ions. Then, we feel justified to use for the other, less-ionized ions the approximate calculations, all fitted following formula (10), with fitting parameters given in tables 8(a) and (b).

4.2. Dielectronic recombination

As already discussed in the introduction, for recombining Na-like to H-like Kr and Mo ions, fitting parameters are available on the University of Strathclyde web site [23]. The recombination rate coefficient α_d (in units of $\text{cm}^3 \text{s}^{-1}$), with T_e in eV, is given by

$$\alpha_d = \frac{1}{T_e^{3/2}} \sum_i C_i \exp\left(\frac{E_i}{T_e}\right) \quad (11)$$

where the *C* and *E* parameters are listed in table 9(a) and (b), respectively, for Kr and Mo, with enough of each coefficient to use the formula down to the low-temperature regime of photoionized plasmas. The given parameters (updated fits C-20060311) refer to the DR totals of the ground level.

The rate coefficients using the *C* and *E* parameters in table 9 (blue full curves) are compared with revised data from [5, 6] (red broken curves for recombining Kr and Mo ions from Na-like to H-like). In figures 11 and 12, six rates of these recombining ions are presented, respectively, for Kr and Mo. Comparison with other available calculations [66–78] is included and detailed in the captions. In [60], coefficients *C* and *E* are also given for recombining Mo ions down to Ar-like. For other, less-ionized ions we found specific calculations in

Table 7. C and E coefficients for evaluating theoretical ionization-rate coefficients of Mo XV–XXXIII according to formula (9). Used are C - and E -values for DI from [6] (first two coefficients) and for ISEA from [60] (third and fourth coefficients).

Z	$C1$	$C2$	$C3$	$C4$
15	1.511×10^4	1.721×10^4		
16	1.203×10^4	1.434×10^4		
17	9.637×10^3	1.197×10^4		
18	7.743×10^3	1.001×10^4		
19	8.368×10^3	6.091×10^3		
20	5.028×10^3	6.987×10^3		
21	4.052×10^3	5.815×10^3		
22	3.262×10^3	4.819×10^3		
23	2.616×10^3	3.966×10^3		
24	2.090×10^3	3.232×10^3	9.343×10^2	2.509×10^2
25	2.635×10^3	1.629×10^3	9.228×10^2	9.827×10^1
26	2.562×10^3	1.107×10^3	4.877×10^2	6.365×10^2
27	2.024×10^3	8.507×10^2	4.800×10^2	6.265×10^2
28	1.556×10^3	6.355×10^2	4.724×10^2	6.166×10^2
29	1.149×10^3	4.561×10^2	4.649×10^2	6.068×10^2
30	1.229×10^3	3.108×10^2	4.576×10^2	5.972×10^2
31	9.614×10^2	1.814×10^2	3.630×10^2	5.231×10^2
32	7.391×10^2	8.550×10^1	2.927×10^2	4.200×10^2
33	5.770×10^2			
Z	$E1$	$E2$	$E3$	$E4$
15	769	2471.9		
16	829.1	2558.4		
17	891.2	2649.7		
18	954.67	2741.1		
19	2833.1	1019.9		
20	1087.5	2930.4		
21	1157.6	3029.7		
22	1230.2	3135.7		
23	1306.5	3247.3		
24	1388.5	3372.9	3362.3	1187.7
25	3509.2	1460.8	3209.1	1417.7
26	2685	1456.3	4719.4	2554.9
27	3784.4	1521.8	4719.4	2554.9
28	3890.9	1590.7	4719.5	2554.9
29	4017.6	1666.3	4719.4	2554.9
30	4189.9	1750.4	4719.5	2554.9
31	4531.7	1844	4959.7	2558.3
32	4936.3	1917.4	4893.4	2591.7
33	5712.7			

the literature for recombining Na-like and Mg-like [78], and for recombining Ni-like ions [79, 80]. For all the other ions, only the BM formula, summed over two resonance transitions (a $\Delta n = 0$ and a $\Delta n = 1$) of the recombining ion, is available. It is known that this formula underestimates the DR rates at low- T_e ; it neglects low-lying autoionizing states since the mean thermal energy of the free electrons is assumed to be at least comparable to the excitation energy of the first resonance transitions of the recombining ion. This has been discussed in

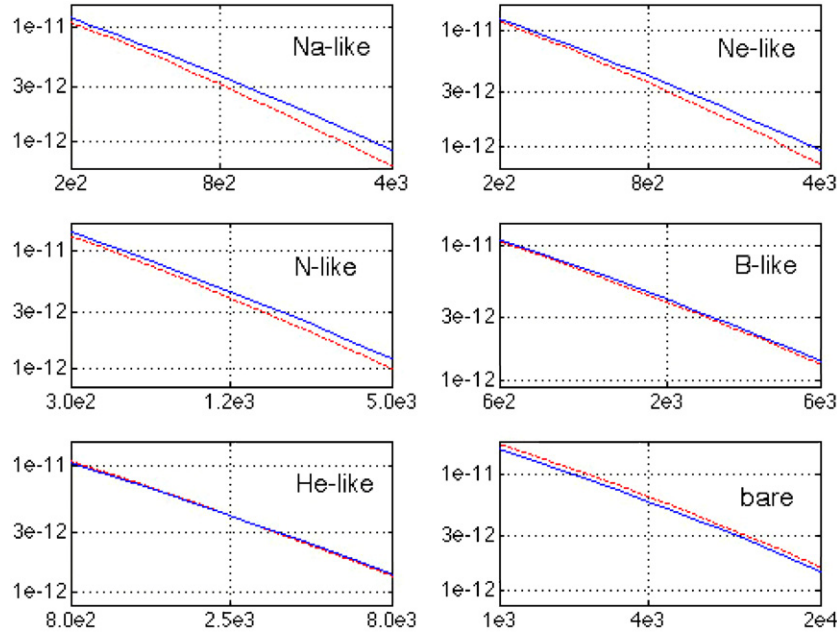


Figure 10. (From left to right and from top to bottom, units $\text{cm}^3 \text{s}^{-1}$ and eV.) Radiative recombination rate coefficients $\alpha_r(T_e)$ for recombining Kr^{25+} , Kr^{26+} , Kr^{29+} , Kr^{32+} , Kr^{34+} , Kr^{36+} ; blue full curves: rates from [23], red broken curves: rates according to the simplified model of recombination into the non-hydrogenic partially filled valence shell and recombination into excited H-like shells, as explained in [27].

detail by Savin *et al* [81, 82] and the reader should refer to their papers. At present, the BM formula is found to be marginally satisfactory for electron-collision-ionized plasmas (i.e., for MCF devices), but not for the low-temperature astrophysical photoionized plasmas.

For recombining Al-like to Ar-like Kr ions we have used the BM formula oscillator strengths f and excitation energies E_{ex} of the resonance transitions (required for the BM formula), which are obtained by the extrapolation of the corresponding values used for ions of elements up to Ge in [2]. On the other hand, for Mo in [60] fit parameters are given down to recombining Ar-like ions. For ions less charged than the Ar-like charge state of both elements, f - and E_{ex} -values were found in the appendix of Post *et al* [3]. Since the average-ion-model energies given by the their code (Adpak) were not available to us, the excitation energies have been taken to be H-like in the oscillator strength $f_{n,n+1}$ formula (see p 436 of [3]). Moreover, for Mo, Mitnik [57] evaluated f and E_{ex} for recombining Mo V to Mo XIX (Sr-like to Cr-like) and these values are preferred to the ones from Adpak. Comparisons of DR rate coefficients for a few Mo ions are shown in figure 13. For Mo XXXI (Mg-like) $\alpha_d(T_e)$ curves from [60, 78] are compared (red full curve and green broken curve respectively). For the other ions, the adopted $\alpha_d(T_e)$ blue curves (full curves, circles and crosses, respectively, for total, $\Delta n = 1$ and $\Delta n = 0$ rates) are compared with the corresponding red curves from Adpak (broken curves, squares and stars, respectively, for total, $\Delta n = 1$ and $\Delta n = 0$ rates). Considering all the ions treated by Mitnik [57], it appears that Adpak is satisfactory for recombining Co-like to Cr-like ions. On the other hand, for recombining Sr-like to Cu-like ions the f - and E_{ex} -values proposed by Mitnik predict a larger ' T_e threshold'. As already said, Mitnik's calculations are preferred to the general ones from Adpak. For recombining Ni-like ions (with only $\Delta n = 1$

Table 8. Fit parameters (A , b , $T0$, $T1$) for the radiative recombination rates of recombined Kr I–XXXVI (a) and Mo I–XLII (b) according to formula (10).

Z	A	b	$T0$	$T1$
(a)				
1	1.674×10^{-13}	-3.559×10^{-1}	1.781×10^0	1.488×10^4
2	6.395×10^{-13}	-3.246×10^{-1}	3.271×10^0	3.093×10^3
3	1.521×10^{-12}	-2.298×10^{-1}	3.924×10^0	2.575×10^3
4	3.989×10^{-12}	1.053×10^{-1}	2.270×10^0	7.712×10^2
5	8.620×10^{-12}	4.060×10^{-1}	1.242×10^0	3.731×10^2
6	9.301×10^{-12}	4.377×10^{-1}	2.047×10^0	4.202×10^2
7	1.664×10^{-11}	5.213×10^{-1}	1.355×10^0	5.051×10^2
8	1.305×10^{-11}	5.616×10^{-1}	3.062×10^0	4.823×10^2
9	5.479×10^{-11}	1.774×10^{-1}	1.663×10^0	8.708×10^2
10	8.928×10^{-11}	3.449×10^{-1}	9.961×10^{-1}	7.278×10^2
11	8.668×10^{-11}	1.343×10^{-1}	1.995×10^0	2.004×10^3
12	8.857×10^{-11}	1.941×10^{-1}	2.337×10^0	2.151×10^3
13	1.158×10^{-10}	4.692×10^{-1}	1.437×10^0	9.265×10^2
14	2.686×10^{-10}	4.730×10^{-1}	5.611×10^{-1}	1.297×10^3
15	2.997×10^{-10}	4.312×10^{-1}	6.742×10^{-1}	1.801×10^3
16	3.532×10^{-10}	5.653×10^{-1}	4.977×10^{-1}	1.295×10^3
17	2.464×10^{-10}	5.540×10^{-1}	1.083×10^0	1.497×10^3
18	2.677×10^{-10}	5.552×10^{-1}	1.181×10^0	1.739×10^3
19	2.215×10^{-10}	5.336×10^{-1}	1.974×10^0	2.194×10^3
20	3.457×10^{-10}	5.665×10^{-1}	1.157×10^0	2.352×10^3
21	3.672×10^{-10}	5.785×10^{-1}	1.239×10^0	2.511×10^3
22	4.016×10^{-10}	5.913×10^{-1}	1.256×10^0	2.687×10^3
23	3.472×10^{-10}	5.868×10^{-1}	1.870×10^0	2.947×10^3
24	6.909×10^{-10}	6.194×10^{-1}	7.191×10^{-1}	3.143×10^3
25	4.936×10^{-10}	5.469×10^{-1}	1.637×10^0	1.254×10^4
26	3.051×10^{-10}	4.446×10^{-1}	4.565×10^0	2.180×10^4
27	6.842×10^{-10}	5.709×10^{-1}	1.283×10^0	1.448×10^4
28	1.033×10^{-9}	6.234×10^{-1}	7.189×10^{-1}	1.221×10^4
29	1.497×10^{-9}	6.596×10^{-1}	4.302×10^{-1}	1.100×10^4
30	2.330×10^{-9}	6.908×10^{-1}	2.267×10^{-1}	1.009×10^4
31	3.422×10^{-9}	7.122×10^{-1}	1.321×10^{-1}	9.539×10^3
32	4.645×10^{-9}	7.261×10^{-1}	8.773×10^{-2}	9.333×10^3
33	1.674×10^{-9}	6.723×10^{-1}	5.891×10^{-1}	1.530×10^4
34	6.300×10^{-10}	5.851×10^{-1}	3.745×10^0	2.706×10^4
35	1.245×10^{-9}	6.716×10^{-1}	1.380×10^0	6.604×10^4
36	3.140×10^{-9}	7.485×10^{-1}	3.048×10^{-1}	7.809×10^4
(b)				
1	1.957×10^{-13}	-5.291×10^{-1}	1.463×10^0	1.338×10^4
2	6.240×10^{-13}	-5.466×10^{-1}	3.553×10^0	1.030×10^4
3	1.471×10^{-12}	-4.586×10^{-1}	4.435×10^0	2.306×10^4
4	2.917×10^{-12}	-3.003×10^{-1}	4.389×10^0	5.209×10^3
5	4.284×10^{-12}	-3.264×10^{-1}	5.733×10^0	2.246×10^4
6	5.520×10^{-12}	-2.934×10^{-1}	7.212×10^0	3.042×10^4
7	1.296×10^{-11}	4.939×10^{-1}	1.895×10^0	5.057×10^2
8	1.231×10^{-11}	3.650×10^{-1}	3.673×10^0	9.595×10^2
9	1.719×10^{-11}	2.832×10^{-1}	3.775×10^0	1.726×10^3
10	2.119×10^{-11}	6.012×10^{-1}	2.857×10^0	6.756×10^2
11	3.238×10^{-11}	3.075×10^{-1}	3.078×10^0	2.695×10^3

Table 8. (Continued.)

<i>Z</i>	<i>A</i>	<i>b</i>	<i>T0</i>	<i>T1</i>
12	7.906×10^{-11}	7.260×10^{-1}	5.463×10^{-1}	7.453×10^2
13	1.018×10^{-10}	7.960×10^{-1}	4.150×10^{-1}	7.186×10^2
14	7.954×10^{-11}	8.113×10^{-1}	8.177×10^{-1}	7.658×10^2
15	1.307×10^{-10}	1.730×10^{-1}	2.878×10^0	3.288×10^3
16	4.548×10^{-10}	3.799×10^{-1}	5.181×10^{-1}	1.864×10^3
17	7.165×10^{-10}	5.847×10^{-1}	1.997×10^{-1}	1.085×10^3
18	5.057×10^{-10}	5.883×10^{-1}	4.042×10^{-1}	1.259×10^3
19	4.193×10^{-10}	5.523×10^{-1}	7.132×10^{-1}	1.612×10^3
20	3.633×10^{-10}	5.573×10^{-1}	1.039×10^0	1.844×10^3
21	4.197×10^{-10}	5.710×10^{-1}	9.768×10^{-1}	2.031×10^3
22	4.314×10^{-10}	5.782×10^{-1}	1.097×10^0	2.238×10^3
23	3.978×10^{-10}	5.782×10^{-1}	1.463×10^0	2.485×10^3
24	4.950×10^{-10}	5.787×10^{-1}	1.230×10^0	2.928×10^3
25	5.303×10^{-10}	5.794×10^{-1}	1.286×10^0	3.416×10^3
26	5.297×10^{-10}	5.856×10^{-1}	1.474×10^0	3.678×10^3
27	7.549×10^{-10}	6.109×10^{-1}	9.434×10^{-1}	3.778×10^3
28	8.507×10^{-10}	6.237×10^{-1}	8.760×10^{-1}	3.967×10^3
29	8.531×10^{-10}	6.280×10^{-1}	9.864×10^{-1}	4.287×10^3
30	9.409×10^{-10}	6.387×10^{-1}	9.420×10^{-1}	4.489×10^3
31	6.295×10^{-10}	5.525×10^{-1}	2.371×10^0	1.591×10^4
32	3.541×10^{-10}	4.350×10^{-1}	7.654×10^0	2.873×10^4
33	8.282×10^{-10}	5.708×10^{-1}	1.938×10^0	1.890×10^4
34	1.256×10^{-9}	6.232×10^{-1}	1.051×10^0	1.622×10^4
35	1.748×10^{-9}	6.593×10^{-1}	6.572×10^{-1}	1.469×10^4
36	2.791×10^{-9}	6.893×10^{-1}	3.275×10^{-1}	1.364×10^4
37	4.461×10^{-9}	7.147×10^{-1}	1.615×10^{-1}	1.276×10^4
38	6.974×10^{-9}	7.318×10^{-1}	8.292×10^{-2}	1.239×10^4
39	1.926×10^{-9}	6.717×10^{-1}	8.602×10^{-1}	2.075×10^4
40	8.161×10^{-10}	5.972×10^{-1}	4.379×10^0	3.493×10^4
41	1.536×10^{-9}	6.764×10^{-1}	1.734×10^0	8.686×10^4
42	3.583×10^{-9}	7.474×10^{-1}	4.316×10^{-1}	1.064×10^5

transitions), Behar's data (green chain curve) [78, 79] are preferred. For all the lowly ionized isosequences of both Kr and Mo, the *C* and *E* coefficients obtained from fits to formula (11) are given in tables 9(a) and (b), respectively, for Kr and Mo. They have been obtained by limiting the minimum temperature in such a way that the fractional abundances of the considered ion were in the range 10^{-4} – 10^{-3} .

We would like to point out that in the web files with the most recent computations N Badnell includes fit coefficients for DR and RR totals from the lowest excited levels. For example, for recombining O-like ions (ground state 3P_2) both metastable levels of the ground term like $^3P_{1,0}$ and metastable terms such as 1D_2 1S_0 are included. We have compared the DR rates from all the included levels for both Kr and Mo. For all the isosequences, above 1 keV (i.e., in the region of electron-collision-dominated plasmas), the rates are all similar (generally differences not greater than 10–20%) with the single exception of the excited 3P_0 level of O-like ions (this being the third ground state level with low statistical weight). On the other hand, at lower photoionized-plasma temperatures the differences can be huge and there are in this T_e region several large differences with the rates reported in the A&A papers

Table 9. *C* and *E* coefficients for dielectronic recombination rates of recombined Kr I–XXXV (a) and Mo I–XLI (b) according to formula (11).

<i>Z</i>	<i>C</i> 1	<i>C</i> 2	<i>C</i> 3	<i>C</i> 4	<i>C</i> 5	<i>C</i> 6	<i>C</i> 7
(a) Kr ions							
1	3.506×10^{-9}						
2	9.914×10^{-9}						
3	1.650×10^{-8}	6.930×10^{-10}					
4	1.870×10^{-8}	1.821×10^{-9}					
5	1.736×10^{-8}	3.636×10^{-9}					
6	7.855×10^{-9}	5.456×10^{-9}					
7	5.545×10^{-9}	-4.990×10^{-12}	7.566×10^{-9}				
8	2.555×10^{-9}	2.518×10^{-8}	7.594×10^{-9}				
9	5.936×10^{-8}	5.297×10^{-8}					
10	7.242×10^{-8}	1.203×10^{-7}					
11	2.751×10^{-7}						
12	3.957×10^{-7}						
13	4.865×10^{-7}						
14	5.813×10^{-7}						
15	5.708×10^{-7}	1.394×10^{-7}					
16	6.700×10^{-7}	1.548×10^{-7}					
17	8.893×10^{-7}						
18	1.139×10^{-6}	4.722×10^{-7}					
19	1.006×10^{-6}	4.371×10^{-7}					
20	9.836×10^{-7}	4.403×10^{-7}					
21	3.592×10^{-8}	8.306×10^{-7}	6.246×10^{-7}				
22	2.279×10^{-7}	6.358×10^{-7}					
23	3.708×10^{-7}	2.883×10^{-7}	5.419×10^{-8}				
24	1.599×10^{-7}	2.133×10^{-6}	2.597×10^{-7}				
25	1.326×10^{-9}	4.784×10^{-8}	1.122×10^{-7}	1.566×10^{-7}	4.699×10^{-7}	1.978×10^{-6}	1.057×10^{-8}
26	2.457×10^{-9}	5.237×10^{-7}	2.397×10^{-6}	4.766×10^{-7}	-7.295×10^{-8}		
27	4.556×10^{-10}	2.475×10^{-9}	1.219×10^{-8}	8.400×10^{-8}	1.283×10^{-6}	2.281×10^{-6}	
28	1.362×10^{-9}	1.190×10^{-8}	3.046×10^{-8}	1.355×10^{-7}	1.145×10^{-6}	2.250×10^{-6}	7.386×10^{-8}
29	3.025×10^{-9}	2.182×10^{-8}	6.246×10^{-8}	1.126×10^{-7}	7.100×10^{-7}	2.854×10^{-6}	
30	1.902×10^{-9}	3.019×10^{-8}	7.424×10^{-8}	1.457×10^{-7}	6.501×10^{-7}	1.902×10^{-6}	1.115×10^{-8}
31	2.431×10^{-9}	3.479×10^{-8}	9.920×10^{-8}	1.981×10^{-7}	7.350×10^{-7}	1.436×10^{-6}	
32	4.914×10^{-9}	1.920×10^{-8}	1.394×10^{-7}	1.890×10^{-7}	5.373×10^{-7}	5.373×10^{-7}	4.509×10^{-7}
33	3.820×10^{-9}	2.453×10^{-8}	9.744×10^{-8}	8.792×10^{-8}	6.338×10^{-7}	6.059×10^{-7}	2.560×10^{-8}
34	3.134×10^{-7}	5.537×10^{-7}	-1.075×10^{-7}				
35	2.142×10^{-7}	2.746×10^{-7}	-2.361×10^{-9}				
<i>Z</i>	<i>E</i> 1	<i>E</i> 2	<i>E</i> 3	<i>E</i> 4	<i>E</i> 5	<i>E</i> 6	<i>E</i> 7
1	1.494×10^0						
2	2.182×10^0						
3	2.649×10^0	6.478×10^1					
4	2.713×10^0	1.056×10^1					
5	2.504×10^0	1.612×10^2					
6	1.970×10^0	1.407×10^1					
7	2.314×10^0	5.340×10^1	1.852×10^1				
8	1.677×10^1	1.568×10^2	4.850×10^1				
9	5.949×10^1	9.735×10^1					
10	7.118×10^1	9.698×10^1					
11	9.074×10^1						
12	9.403×10^1						
13	9.343×10^1						
14	8.893×10^1						
15	8.683×10^1	1.419×10^2					
16	8.494×10^1	1.567×10^2					
17	8.294×10^1						
18	9.659×10^1	2.415×10^2					
19	9.943×10^1	2.704×10^2					
20	9.826×10^1	2.673×10^2					

Table 9. (Continued.)

<i>Z</i>	<i>E1</i>	<i>E2</i>	<i>E3</i>	<i>E4</i>	<i>E5</i>	<i>E6</i>	<i>E7</i>
(a) Kr ions							
21	4.760×10^1	8.484×10^1	2.590×10^2				
22	5.336×10^1	1.243×10^2					
23	5.371×10^1	1.572×10^2	3.633×10^3				
24	4.386×10^1	1.331×10^3	3.815×10^2				
25	2.727×10^0	9.651×10^0	3.494×10^1	7.749×10^1	5.359×10^2	1.430×10^3	1.989×10^4
26	4.440×10^2	6.726×10^2	1.324×10^3	2.791×10^3	6.394×10^3		
27	1.366×10^0	1.196×10^1	3.538×10^1	2.175×10^2	8.541×10^2	1.670×10^3	
28	1.433×10^0	1.013×10^1	4.208×10^1	2.059×10^2	8.462×10^2	1.636×10^3	4.079×10^3
29	2.291×10^0	1.050×10^1	3.995×10^1	1.346×10^2	6.349×10^2	1.616×10^3	
30	1.455×10^0	1.196×10^1	4.377×10^1	1.585×10^2	7.836×10^2	1.758×10^3	1.298×10^5
31	1.289×10^0	1.424×10^1	5.099×10^1	1.698×10^2	8.962×10^2	1.875×10^3	
32	8.412×10^{-1}	1.296×10^1	6.251×10^1	2.746×10^2	1.593×10^3	1.593×10^3	9.850×10^3
33	4.343×10^0	1.432×10^1	6.952×10^1	4.209×10^2	1.685×10^3	9.944×10^3	3.166×10^4
34	9.005×10^3	1.209×10^4	1.320×10^4				
35	9.195×10^3	1.226×10^4	1.728×10^4				
<i>Z</i>	<i>C1</i>	<i>C2</i>	<i>C3</i>	<i>C4</i>	<i>C5</i>	<i>C6</i>	<i>C7</i>
(b) Mo ions							
1	1.842×10^{-10}	1.299×10^{-8}					
2	6.827×10^{-10}	3.548×10^{-8}					
3	1.685×10^{-9}	7.231×10^{-8}					
4	2.200×10^{-7}						
5	3.475×10^{-7}						
6	5.083×10^{-7}	1.434×10^{-7}					
7	5.135×10^{-7}	2.591×10^{-7}					
8	4.845×10^{-7}	4.167×10^{-7}					
9	4.133×10^{-7}	6.207×10^{-7}					
10	3.006×10^{-7}	8.758×10^{-7}					
11	1.662×10^{-7}	1.145×10^{-6}					
12	2.910×10^{-7}	1.557×10^{-6}					
13	1.329×10^{-7}	2.247×10^{-6}					
14	8.782×10^{-9}	4.353×10^{-7}	7.870×10^{-8}				
15	1.011×10^{-7}	1.261×10^{-6}					
16	2.211×10^{-7}	1.427×10^{-6}					
17	4.202×10^{-7}	1.390×10^{-6}					
18	5.873×10^{-7}	1.471×10^{-6}					
19	6.349×10^{-7}	2.573×10^{-7}					
20	7.612×10^{-7}	2.746×10^{-7}					
21	9.267×10^{-7}	2.910×10^{-7}					
22	1.033×10^{-6}	3.112×10^{-7}					
23	1.302×10^{-6}	1.986×10^{-7}					
24	6.170×10^{-7}	3.531×10^{-7}	6.805×10^{-7}	8.002×10^{-7}	1.089×10^{-6}		
25	9.452×10^{-7}	4.169×10^{-7}	6.032×10^{-7}	1.048×10^{-6}	1.132×10^{-6}		
26	1.021×10^{-6}	4.827×10^{-7}	6.410×10^{-7}	3.965×10^{-7}	9.822×10^{-7}	9.393×10^{-7}	
27	9.905×10^{-7}	4.681×10^{-7}	5.664×10^{-7}	1.262×10^{-6}	1.740×10^{-6}		
28	8.892×10^{-7}	4.202×10^{-7}	4.813×10^{-7}	1.570×10^{-6}	2.176×10^{-6}		
29	7.255×10^{-7}	3.429×10^{-7}	3.857×10^{-7}	1.881×10^{-6}	1.791×10^{-6}		
30	5.060×10^{-7}	2.022×10^{-7}	2.360×10^{-7}	2.837×10^{-6}	1.805×10^{-6}		
31	1.005×10^{-8}	3.982×10^{-8}	2.430×10^{-7}	1.982×10^{-7}	8.056×10^{-7}	2.856×10^{-6}	2.192×10^{-8}
32	5.690×10^{-9}	8.272×10^{-7}	3.151×10^{-6}	6.676×10^{-7}	-9.136×10^{-8}		
33	1.153×10^{-9}	1.580×10^{-8}	2.174×10^{-8}	1.660×10^{-7}	1.898×10^{-6}	2.818×10^{-6}	
34	6.473×10^{-9}	2.474×10^{-8}	6.650×10^{-8}	2.358×10^{-7}	1.897×10^{-6}	2.618×10^{-6}	1.834×10^{-8}
35	2.229×10^{-9}	3.997×10^{-8}	1.037×10^{-7}	2.140×10^{-7}	1.310×10^{-6}	3.309×10^{-6}	
36	4.395×10^{-8}	3.210×10^{-8}	1.327×10^{-7}	2.290×10^{-7}	1.043×10^{-6}	2.331×10^{-6}	
37	6.494×10^{-9}	4.630×10^{-8}	1.508×10^{-7}	2.930×10^{-7}	8.848×10^{-7}	1.935×10^{-6}	
38	1.743×10^{-8}	6.546×10^{-8}	9.000×10^{-8}	2.225×10^{-7}	2.982×10^{-7}	1.310×10^{-6}	4.958×10^{-7}
39	3.162×10^{-8}	1.829×10^{-8}	1.008×10^{-7}	1.096×10^{-7}	5.437×10^{-7}	4.102×10^{-7}	6.058×10^{-7}

Table 9. (Continued.)

<i>Z</i>	<i>C1</i>	<i>C2</i>	<i>C3</i>	<i>C4</i>	<i>C5</i>	<i>C6</i>	<i>C7</i>
(b) Mo ions							
40	3.699×10^{-7}	4.037×10^{-7}	4.317×10^{-8}	1.645×10^{-9}			
41	2.221×10^{-7}	2.880×10^{-7}	1.038×10^{-9}				
<i>Z</i>	<i>E1</i>	<i>E2</i>	<i>E3</i>	<i>E4</i>	<i>E5</i>	<i>E6</i>	<i>E7</i>
1	1.494×10^0	6.974×10^0					
2	2.961×10^0	7.895×10^0					
3	4.877×10^0	1.073×10^1					
4	3.846×10^1						
5	3.874×10^1						
6	3.877×10^1	2.635×10^2					
7	3.999×10^1	2.681×10^2					
8	4.110×10^1	2.717×10^2					
9	4.207×10^1	2.748×10^2					
10	4.297×10^1	2.781×10^2					
11	4.382×10^1	2.779×10^2					
12	2.820×10^1	2.841×10^2					
13	2.714×10^1	2.876×10^2					
14	2.576×10^1	2.474×10^2	8.929×10^1				
15	1.433×10^2	3.047×10^2					
16	1.388×10^2	3.222×10^2					
17	1.342×10^2	3.410×10^2					
18	1.318×10^2	3.572×10^2					
19	1.169×10^2	2.100×10^2					
20	1.116×10^2	2.288×10^2					
21	1.103×10^2	2.486×10^2					
22	1.068×10^2	2.688×10^2					
23	1.031×10^2	6.946×10^2					
24	5.729×10^2	8.814×10^1	5.721×10^1	1.689×10^3	2.491×10^3		
25	4.186×10^2	7.608×10^1	6.122×10^1	1.705×10^3	2.624×10^3		
26	4.404×10^2	4.332×10^1	4.428×10^1	1.094×10^3	2.394×10^3	1.832×10^3	
27	4.404×10^2	4.332×10^1	4.428×10^1	1.340×10^3	2.498×10^3		
28	4.404×10^2	4.332×10^1	4.428×10^1	1.339×10^3	2.493×10^3		
29	4.404×10^2	4.332×10^1	4.428×10^1	1.339×10^3	2.492×10^3		
30	4.859×10^2	3.687×10^1	3.850×10^1	2.458×10^3	1.278×10^3		
31	2.779×10^0	1.107×10^1	5.064×10^1	1.167×10^2	6.861×10^2	1.959×10^3	4.231×10^4
32	5.965×10^2	8.962×10^2	1.809×10^3	3.885×10^3	1.015×10^4		
33	1.163×10^0	1.148×10^1	7.714×10^1	3.422×10^2	1.173×10^3	2.339×10^3	
34	2.827×10^0	1.099×10^1	6.814×10^1	3.038×10^2	1.197×10^3	2.415×10^3	6.599×10^4
35	1.252×10^1	2.825×10^1	6.793×10^1	2.282×10^2	9.850×10^2	2.305×10^3	
36	3.216×10^0	1.173×10^1	6.497×10^1	2.246×10^2	1.067×10^3	2.462×10^3	
37	1.749×10^0	1.680×10^1	6.539×10^1	2.169×10^2	1.059×10^3	2.501×10^3	
38	3.405×10^0	1.154×10^1	6.442×10^1	1.636×10^2	6.852×10^2	2.335×10^3	1.473×10^4
39	2.937×10^0	1.596×10^1	7.245×10^1	2.309×10^2	1.544×10^3	3.853×10^3	1.573×10^4
40	1.236×10^4	1.580×10^4	1.966×10^4	7.924×10^4			
41	1.256×10^4	1.658×10^4	3.589×10^4				

and the revised values in the errata as well. Performing the same comparison for RR, the conclusion is the same; only when moving below 1 keV do the RR rates of the included levels of a particular ion diverge with decreasing T_e .

In [5, 6], collisional-radiative models are used for evaluating the excited-state populations and to compute radiative losses. For L-shell Kr and Mo ions, at T_e -values where these ions are highly populated and for n_e -values typical of MCF devices, these models give low excited-level population fractions, giving another justification of using ground level RR+DR rates.

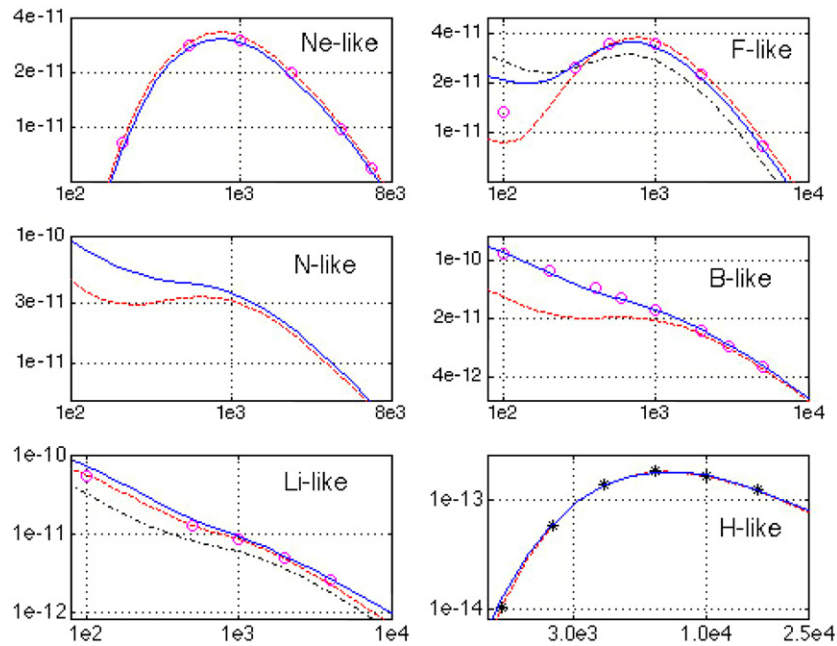


Figure 11. (From left to right and from top to bottom, units $\text{cm}^3 \text{s}^{-1}$ and eV.) Dielectronic recombination rate coefficients $\alpha_d(T_e)$ for recombining Kr^{26+} , Kr^{27+} , Kr^{29+} , Kr^{31+} , Kr^{33+} , Kr^{35+} ; blue full curves: rates from [23], red broken curves: rates from [5]. References for other colours for the indicated recombining sequences. Ne-like: magenta circles [77]; F-like magenta circles [75], black chain [76]; B-like magenta circles [72], Li-like magenta circles [69], black chain [70]; H-like black stars [66].

5. Charge-state distribution at ionization equilibrium

In the previous sections, we have collected data on recombination and ionization of Kr and Mo and the proposed fit coefficients are presented in tables 1–9. When ionization experimental cross sections are available (Kr I–VI, Kr VIII–XIX and Mo I–IX), the ionization-rate coefficients obtained by integration over a Maxwellian electron distribution are proposed (tables 1–3); for the remaining Kr ions the fitted rate coefficients tabulated in [21] for all the 36 ions should be used (table 5). For Mo, contrary to Kr, the corresponding rate coefficients for the 42 Mo ions are not available at the moment. The proposed data are from Mitnik *et al* [52, 53, 57, 58] for Mo X–XIV (As-like to Cu-like ions in table 6) and from LLNL [6, 60] for Mo XV–XXXIII (Ni-like to Ne-like ions in table 7). The contribution of ISEA is missing for Mo XV–XXIII (Ni-like to Ca-like), but it can be neglected for these sequences by comparison with the calculations for the corresponding Kr IX–XVII. For Mo XXXIV–XLII (F-like to H-like), Lotz’s formula (8) can be used.

For RR and DR the recommended data are respectively in tables 9 and 10. For highly ionized recombining ions from the Na-like sequence the data available on the University of Strathclyde web site from the coordinated programme are given. For RR of the lowly ionized ions the simple, coarse approximation of recombination into a partially filled valence band and into H-like excited levels is considered [27]. For DR of the lowly ionized ions, the general BM formula is used [25, 26] unless few detailed calculations exist.

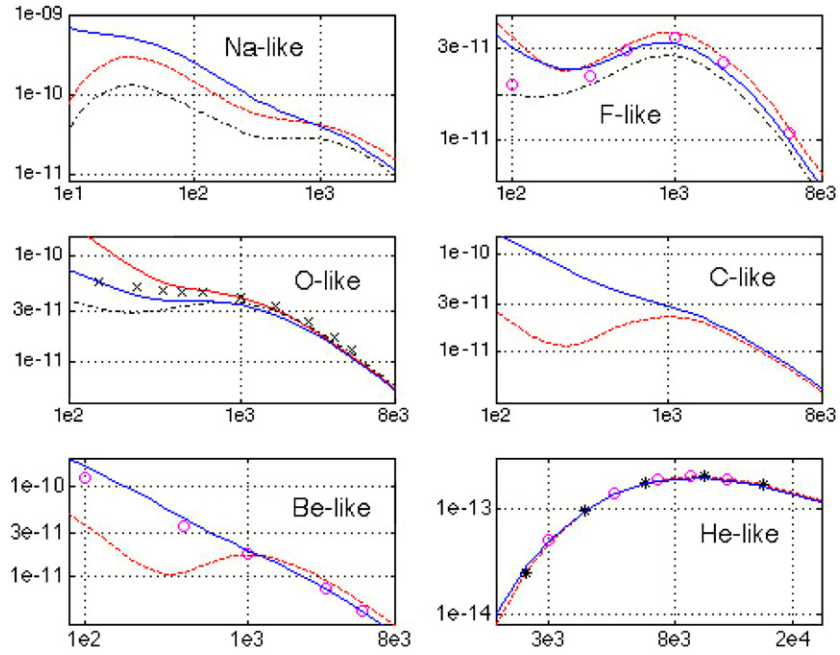


Figure 12. (From left to right and from top to bottom, units $\text{cm}^3 \text{s}^{-1}$ and eV.) Dielectronic recombination rate coefficients $\alpha_d(T_e)$ for recombining Mo^{31+} , Mo^{33+} , Mo^{34+} , Mo^{36+} , Mo^{38+} , Mo^{40+} . References for other colours for the indicated recombining sequences. Na-like black chain [78]; F-like magenta circles [75], black chain [76], O-like black chain [74], black crosses [73], Be-like magenta circles [71], He-like magenta circles [68], black stars [67].

The data proposed allow straightforward determination of the CSD at ionization equilibrium, i.e., the ionic fractions or fractional abundances f_Z as a function of T_e . Tables of $f_Z(T_e)$ are given in tables 10 and 11, respectively, for Kr and Mo (stacks.iop.org/JPhysB/39/4457).

These CSDs have been compared with the corresponding CSDs of [5 and 6]. The $f_Z(T_e)$ curves are shown for a few selected Kr and Mo ions, respectively, in figures 14 and 15 (blue full and red broken lines, respectively, for the present calculations and those from [5 and 6]). For both elements in the 1–10 keV T_e range (upper panels of both figures), where the main change was the introduction of the RR+DR rates from the Strathclyde web site, the differences are not large. The other three T_e ranges (two for Kr and one for Mo) are chosen to show the effect of replacing old theoretical ionization rates with the rates deduced from experimental cross-section data (up to Kr XIX and to Mo IX). Remember that, in figures 6 and 7, the recent rates from [21] have also been compared with the experimental rates for isosequences up to Kr XIX. For both elements, in the T_e ranges below ~ 1 keV shown in figures 14 and 15, the $f_Z(T_e)$ curves are clearly shifted towards lower T_e -values when the available experimental ionization cross sections are used.

6. Re-analysis of a JET Mo–Ge laser blow-off injection

In MCF devices, the $f_Z(T_e)$ curves give a first indication of the CSD when the electron temperature T_e is known. However, the CSD is modified by plasma transport perpendicularly to the flux surfaces. If the movement is towards increasing T_e , the CSD is lower than at IE and

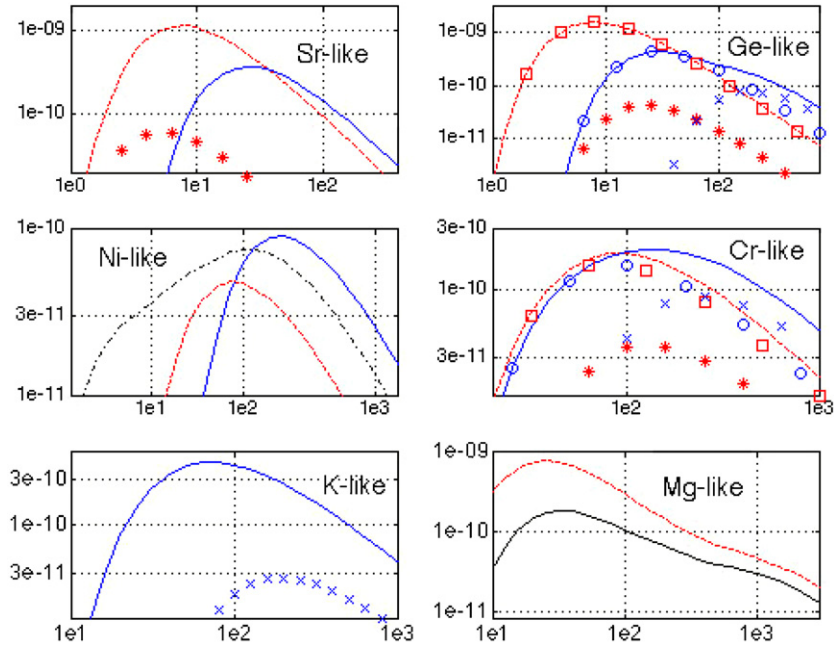


Figure 13. (From left to right and from top to bottom, units $\text{cm}^3 \text{s}^{-1}$ and eV.) Dielectronic recombination rate coefficients $\alpha_d(T_e)$ for recombining Mo^{4+} , Mo^{10+} , Mo^{14+} , Mo^{18+} , Mo^{23+} , Mo^{30+} ; blue: rates using BM formula with f and E_{ex} as proposed by Mitnik *et al* [57] (full curves total rates, circles $\Delta n = 0$, crosses $\Delta n = 1$ transitions); red: rates using BM formula with f and E_{ex} from Adpak [3] (full curves total rates, squares $\Delta n = 0$, stars $\Delta n = 1$ transitions) for Ni-like ions black chain rates from Behar [79, 80], for Mg-like red broken and black full, respectively, from [6] and [78].

the plasma is in an ionizing state. On the other hand, if the movement is towards decreasing T_e , the CSD is higher than at IE and the plasma is in a recombining state. Impurity ion-transport codes are available, describing ionization, recombination and radial transport of the ions of a given impurity species. They require as input data the radial profiles of the electron temperature $T_e(r)$ and of the electron density $n_e(r)$, which are needed to evaluate ionization and recombination rate coefficients, and two transport coefficients, a diffusion coefficient $D(r)$ and a convection velocity $V(r)$. In most cases (e.g., when only a few strong line brightnesses are available), atomic data are assumed to be valid and the simulations are used to give $D(r)$ and $V(r)$. However, with high quality and large quantities of spectroscopic data, it is possible to go further and to verify atomic data (i.e., S_{ion} and $\alpha_{\text{rec}} = \alpha_r + \alpha_d$).

To the best of our knowledge, the first of such comparisons has been reported by May *et al* [83], analysing space-resolved distributions of laser blow-off (LBO) injections of Fe and Ge ions and of intrinsic Ni ions in the FTU tokamak. Using data from [1] for Fe and Ni and from [2] for Ge, the F-like to B-like charge states could not be simulated unless the relevant $\alpha_{\text{rec}}/S_{\text{ion}}$ ratios were increased. In another paper on M-shell Ni spectra in the 144–180 Å region [84], both $D(r)$ and $V(r)$ were known from similar discharges and with fits on the strongest lines of the observed Ni X–XV ions, the best sets of data for both ionization and recombination have been deduced.

As an example of verification of Mo atomic data, the simulation of a JET LBO injection from a composite Mo–Ge target into a 3 MA discharge heated by a 8 MW ion cyclotron

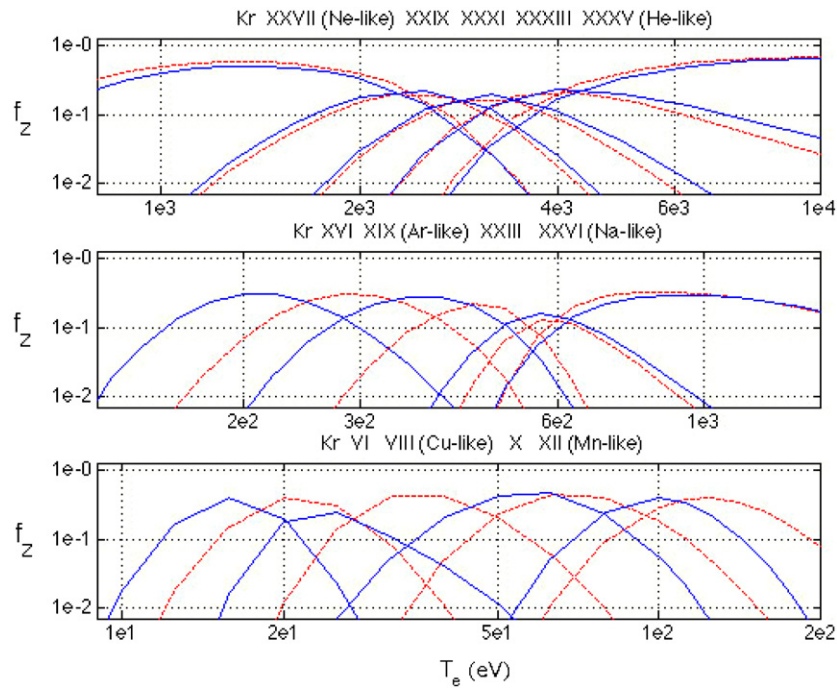


Figure 14. Fractional abundances $f_Z(T_e)$ curves for a few selected Kr ions: blue full and red broken lines show, respectively, the present calculations and those from [5]. See also the text for explanations.

resonance heating pulse ($T_e(0) \sim 6$ keV, $n_e(0) \sim 3.5 \times 10^{19} \text{ m}^{-3}$) is presented. Along with low resolution 100–300 Å spectra, L-shell (35–50 Å) Mo spectra and 65–95 Å spectra (including both M-shell Mo and L-shell Ge lines) are available. For the spectral analysis, intrinsic C and Be lines have been subtracted from the data from pre-injection spectra.

The transport coefficients $D(r)$ and $V(r)$ have been obtained by simulations of Mo and Ge line brightnesses and of the central brightnesses of the soft x-ray (SX) signals. First, the boundary condition (source function) of the incoming neutral flux is adjusted to follow the lowest ionization stages observed (Mo XXIV 72.1 Å, Mo XXV 74.2 and Ge XXI 196 Å). Then, $D(r)$ and $V(r)$ are varied to obtain the best simulation of the time histories of several observed lines. To simulate closely the outflow of as many as possible ionization stages, the simulation requires a time-dependent $V(r)$. In figure 16, $D(r)$ and $V(r)$ ($V(r)$ at two different times) are shown for the Mo simulation. They show the presence of both a peripheral barrier at the plasma edge (produced by reducing D and by increasing V inward near the last closed flux surface) and of an improved-confinement core region. The simulations of Mo XXXI 116 Å and Mo XXXII 128 Å signals are critical for demonstrating the former phenomenon, the peripheral barrier, while the simulation of the relatively long decay of the of F-like Mo XXXIV 37.6 Å line (blended with a O-like line) is essential for demonstrating the latter, the high confinement region in the core. The simulation of the observed Ge line brightnesses requires a slight increase of the D -values found to be optimal for Mo, both in the central region and at the peripheral barrier. Examples of normalized-brightness histories are given in figure 17, with blue full and red broken lines, respectively, for experiment and simulations.

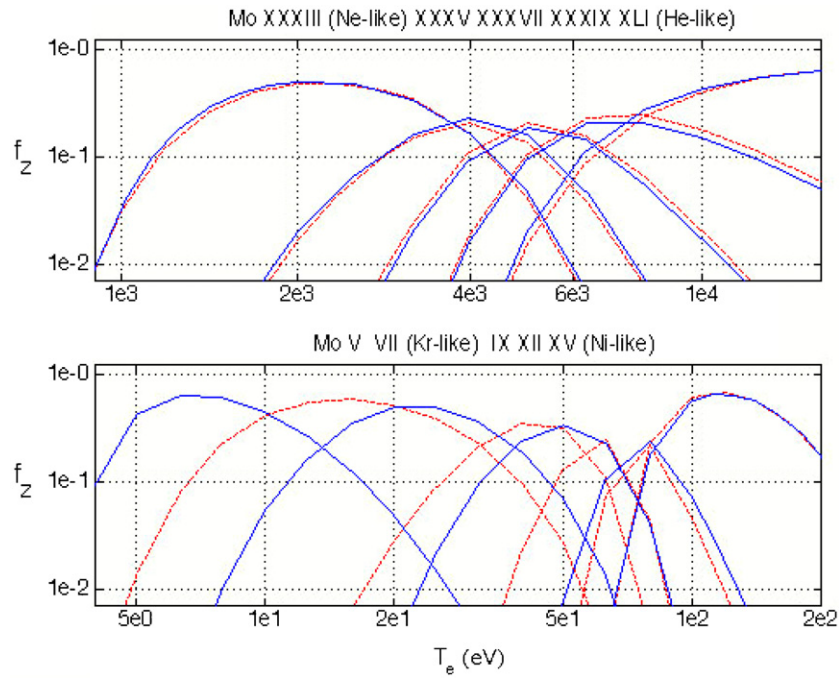


Figure 15. Fractional abundances $f_Z(T_e)$ curves (with T_e in eV) for a few selected Mo ions: blue full and red broken lines show, respectively, the present calculations and those from [6]. See also the text for explanations.

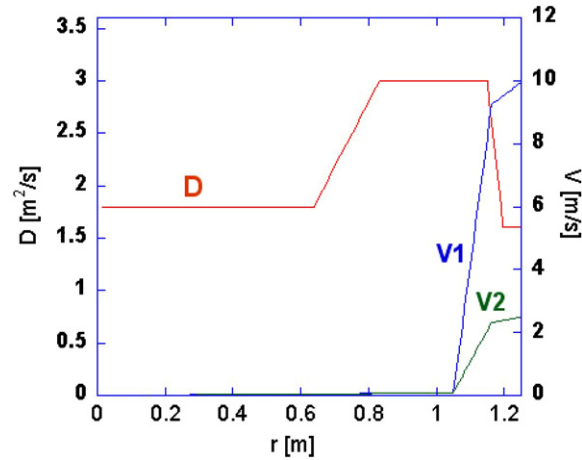


Figure 16. $D(r)$ and $V(r)$ radial profiles (units $\text{m}^2 \text{s}^{-1}$ and m s^{-1}). To simulate closely the outflow of as many as possible ionization stages, the simulation requires a time-dependent $V(r)$. Critical for it is the simulation of the SX brightness. Shown are the limit profiles: V1 up to 100 ms and V2 between 300 and 600 ms after the injection. Inward velocities are positive.

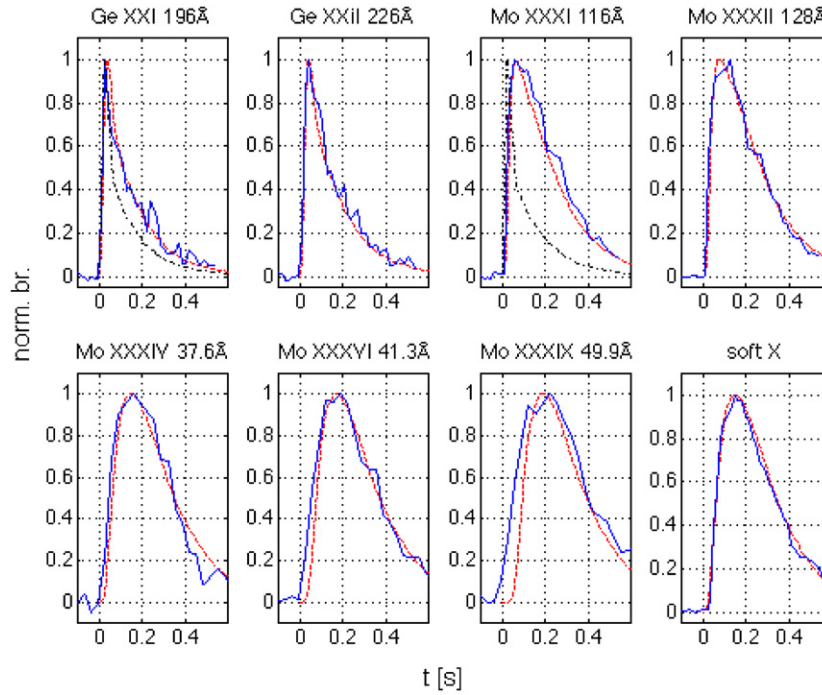


Figure 17. Experimental (blue full line) and simulated (red broken line) normalized brightnesses as a function of time t (s). The additional black chain lines (superposed to the Mo XXXI and to the Ge XXI lines) show the lowly ionized Mo XIII and Ge XV line brightnesses, following the incoming neutral flux (a triangular pulse followed by an exponentially decaying tail).

The relative amplitudes of the lines from different ionization stages depend on the transport parameters and on the atomic rates.

After the evaluation of radial CSD, post-process subroutines are used to produce simulated spectra, using line photon emission coefficients (PECs) from collisional-radiative models (CRM). The PECs have been obtained using the HULLAC code, as discussed, for example, in [84].

To verify the atomic data, we find the best fits of the simulated spectra to the peaks of the strongest lines (i.e., to the main contributors to the detected spectra). If $sp_{exp}(\lambda)$ and $sp_{sim}(\lambda)$ are, respectively, the normalized experimental and simulated spectra, C_{mult} is a multiplicative constant, whose value is obtained by the minimization of $\sum_i (C_{mult} sp_{sim}(\lambda_i) - sp_{exp}(\lambda_i))^2$ over the selected lines. The ‘best’ spectra are the ones with the lowest estimated sample deviation (sdev) defined as the square root of the sum to be minimized.

The 35–50 Å experimental spectrum, obtained 200 ms after the LBO injection, is shown (blue full line) in figure 18. The initial simulated spectrum (not plotted) shows B-like and Be-like ion lines clearly stronger than found experimentally. It is then necessary to modify either the recombination or the ionization rates of the involved isosequences to reduce the core ionization degree.

The simulation obtained with the lowest sample deviation (sdev = 0.205) is shown in figures 18 (red broken line), slightly shifted towards shorter wavelengths for clearness in the comparison with the experimental spectrum (blue full line). It has been obtained by multiplying, for recombining F-like to Be-ions, the α_{rec} rates by the following multiplicative factors $f = 0.95, 1.0, 1.6, 1.85, 1.2, 1.3$. To give an idea of the uncertainties of the f -factors,

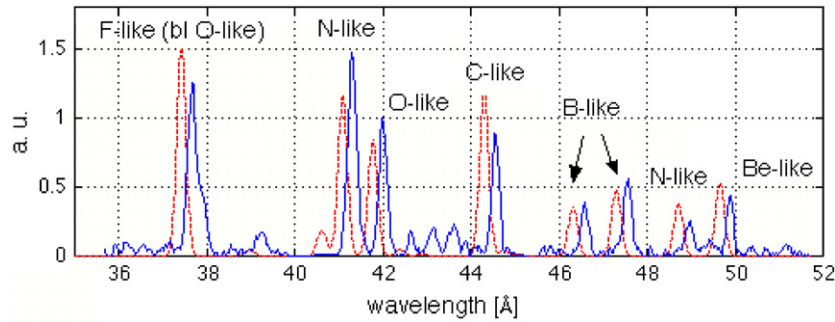


Figure 18. Experimental (blue full line) and simulated (red broken line) normalized spectra as a function of wavelength (Å), 200 ms after the LBO injection. For clearness, the simulated spectrum has been slightly shifted towards the shorter wavelengths. The recombination rates of the strongest lines of the six shown isosequences have been increased as explained in the text.

another simulation ($f = 1.0, 1.1, 1.6, 1.8, 1.25, 1.25$, $\text{sdev} = 0.235$) would give a simulated red broken curve practically coincident with the one shown in figure 18. The simulations are practically equivalent (i.e., with practically the same estimated sample deviation), if the S_{ion} rates for ionizing Ne-like to B-like ions are reduced by dividing them by f . To be precise, the simulation could be even judged better, since the sample deviations are generally reduced by 0.1–0.15. Incidentally, the considered variations of either α_{rec} or S_{ion} have negligible effects on the normalized simulated brightness histories of figure 17.

A question now arises: is the simulation of Mo L-shell spectra improved when using the proposed new data instead of using the old data from [6]? For the involved Mo ions, the S_{ion} rates are the same, but the DR rates come from the Strathclyde web site. The differences between the two used samples of DR rates can be seen in figure 12 (blue and red curves). Moreover, the upper panel of figure 15 shows that the CSD are not much different in the keV T_e range. We have repeated the LBO simulation with the old data. The simulated spectra are practically the same for the lowest sample standard deviations. For example, with $f = 1.0, 1.0, 1.7, 1.9, 1.3, 1.3$, $\text{sdev} = 0.22$. With both samples of rates the largest f -values are either for recombining N-like and C-like ions or for ionizing O-like and N-like ions. It is, however, necessary to wait for new experimental data before we should propose corrections to the corresponding assessed rates.

7. Conclusion

Atomic data for both ionization and recombination of Kr and Mo ions are reviewed, the rates for these processes needing to be regularly updated following the publication of new theoretical calculations and new experimental data. The proposed rates have been summarized at the beginning of section 5, before the evaluations of the fractional abundances of the ions of each element. Only ionizing electron collisions and both radiative and dielectronic recombination processes are considered. Processes neglected are photoionization, photoabsorption, electron impact multiple ionation, three-body recombination, electron-density effects both in ionization and in dielectronic recombination and, finally, charge-exchange (CX) reactions of the plasma ions with neutral-hydrogen isotopes. Except for the last two, these processes can be neglected in MCF devices. CX reactions reduce the ionization degree and are a supplementary recombination process included, if necessary, in the simulation codes. For the two elements considered in this paper only scaled cross sections versus scaled energy are available (see, e.g.,

the references quoted in the last section of [2]). Multiple ionization, for which experimental data exist for a few lowly ionized Kr and Mo ions, can be neglected in MCF devices. This has been shown in the simulations of [85] and it is due to the fact that, at the edge, the ions are located in layers with T_e -values near the single ionization potentials while multiple ionization has a larger threshold. On the other hand, if neutrals or lowly ionized ions are suddenly exposed to high T_e -values, multiple ionization could influence the charge-state evolution. This is possible in MCF devices with laser blow-off or pellet impurity injections, but no reliable spectroscopic measurements on the initial interaction region are available.

The necessity of corrections to the proposed DR rates is in some way an open question. The rates are first decreased by the ionization of the singly excited states, i.e. the non-autoionizing states following stabilization. They are then decreased with increasing n_e . Moreover, as treated, for example, in [86], there is some enhancement due to l-mixing of autoionizing states by electric field (Stark effect) and/or by collisions, but probably not enough to bring it back to the zero-density value. The influence of the electric field has been clearly observed in several DR experiments, but the plasma microfields or turbulent fields are hardly known. The picture is further complicated by the discovery that magnetic fields, crossed with electric fields, reduce in most cases the electric field enhancement [22]. A correction formula for the n_e influence had proposed long time ago in [3], but, as far as we know, at present, the DR rates included in the simulation codes do not consider any influence of the electron density or that of the electric fields. The corresponding effect on the ionization rates increased through the ionization of the excited states is considered marginal at the densities of the MCF devices.

To conclude, we believe that the data collected represent the state of the art for ionization and recombination rates for Kr and Mo ions. In most cases (e.g., when only a few strong line brightnesses are available), atomic data are often assumed to be valid and the simulations are used to give the transport parameters ($D(r)$ and $V(r)$). However, with high quality spectra that contain lines from many charge states it will be possible to go further and to verify the atomic data used (i.e., the ionization and recombination rates). As an example, the simulation of a JET Mo LBO injection was re-analysed with the revised rates and multiplicative correction factors are obtained for the ratios of recombination over ionization rates for L-shell ions.

Acknowledgments

One of the authors (MM) wishes to thank Professor Nigel Badnell for many useful interactions through e-mails and for placing him on the mailing list for announcing new releases on the University of Strathclyde web site. This work was performed under the auspices of the US Department of Energy by Lawrence Livermore National Laboratory under contract no W-7405ENG-48.

References

- [1] Mazzotta P *et al* 1998 *Astron. Astrophys. Suppl.* **133** 403
- [2] Mazzitelli G and Mattioli M 2002 *At. Data Nucl. Data Tables* **82** 313
- [3] Post D *et al* 1977 *At. Data Nucl. Data Tables* **20** 397
- [4] Post D *et al* 1995 *Phys. Plasmas* **2** 2328
- [5] Fournier K *et al* 2000 *Nucl. Fusion* **40** 847
- [6] Fournier K *et al* 1997 *Nucl. Fusion* **37** 825
- Fournier K *et al* 1998 *Nucl. Fusion* **38** 639 (erratum)
- [7] Ongena J *et al* 1999 *Plasma Phys. Control. Fusion* **41** A379
- [8] Maddison G *et al* 2003 *Nucl. Fusion* **43** 49
- [9] Jackson G *et al* 2002 *Plasma Phys. Control. Fusion* **44** 1893

- [10] Rapp J *et al* 1997 *Plasma Phys. Control. Fusion* **39** 1615
- [11] May M *et al* 2000 *Phys. Rev. E* **61** 3042
- [12] May M *et al* 1999 *Plasma Phys. Control. Fusion* **41** 45
- [13] Philipps V *et al* 1994 *Nucl. Fusion* **34** 1417
- [14] Rice J *et al* 1996 *J. Phys. B: At. Mol. Opt. Phys.* **29** 2191
- [15] May M *et al* 1997 *Nucl. Fusion* **37** 881
- [16] Carraro L *et al* 2004 *Plasma Phys. Control. Fusion* **46** 389
- [17] Pacella D *et al* 2000 *Phys. Rev. E* **61** 5701
- [18] Mattioli M *et al* 2004 *31st EPS Conf. on Plasma Phys. (London)* ECA 28G P-1.150
- [19] Dux R *et al* 1999 *Nucl. Fusion* **39** 1509
- [20] Dux R *et al* 2004 *Nucl. Fusion* **44** 260
- [21] Loch S *et al* 2002 *Phys. Rev. A* **66** 02708
- [22] Badnell N *et al* 2003 *Astron. Astrophys.* **406** 1151
- [23] <http://amdpp.phys.strath.ac.uk/tamoc/DR> and [/tamoc/RR](http://amdpp.phys.strath.ac.uk/tamoc/RR)
- [24] Badnell N *Astrophys. J. Suppl.* accepted Preprint [astro-ph/0604144](http://arxiv.org/abs/astro-ph/0604144)
- [25] Burgess A 1965 *Astrophys. J.* **141** 1588
- [26] Merts A, Cowan R and Magee N 1976 *Los Alamos Report* LA-6260-MS
- [27] De Michelis C and Mattioli M 1981 *Nucl. Fusion* **21** 677
- [28] Krishnakumar E and Srivastava S 1988 *J. Phys. B: At. Mol. Opt. Phys.* **21** 1055
- [29] Wetzel R *et al* 1987 *Phys. Rev. A* **35** 559
- [30] Man K, Smith A and Harrison M 1987 *J. Phys. B: At. Mol. Phys.* **20** 5865
- [31] Man K, Smith A and Harrison M 1993 *J. Phys. B: At. Mol. Phys.* **26** 1365
- [32] Tinschert K *et al* 1987 *J. Phys. B: At. Mol. Phys.* **20** 1121
- [33] Gregory D 1985 *Nucl. Instrum. Methods Phys. Res. B* **10/11** 87
- [34] Gregory D, Dittner P and Crandall D 1983 *Phys. Rev. A* **27** 724
- [35] Bannister M, Guo X and Kojima T 1994 *Phys. Rev. A* **49** 4676
- [36] Bannister M *et al* 1988 *Phys. Rev. A* **38** 38
- [37] Teng H *et al* 2000 *J. Phys. B: At. Mol. Opt. Phys.* **33** 467
- [38] Khouilid M *et al* 2001 *J. Phys. B: At. Mol. Opt. Phys.* **34** 1727
- [39] <http://www-cfadc.phy.ornl.gov/xbeam>
- [40] Higgins M *et al* 1989 *Culham Laboratory Report* CLM-R294, data also available on <http://www-cfadc.phy.ornl.gov/aladdin/aladdin.list.html>
- [41] Bartlett P and Stelbovics A 2004 *At. Data Nucl. Data Tables* **86** 235
- [42] Younger S 1981 *J. Quantum Spectrosc. Radiat. Transfer* **26** 329
- [43] Arnaud M and Raymond J 1992 *Astrophys. J.* **398** 394
- [44] Chen M and Reed K 1993 *Phys. Rev. A* **47** 1874
- [45] Gorczyca T *et al* 1994 *Phys. Rev. A* **49** 4682
- [46] Pindzola M *et al* 1987 *Nucl. Fusion Suppl.* 21
- [47] Pindzola M *et al* 1991 *Phys. Scr.* **T37** 35
- [48] Man K, Smith A and Harrison M 1987 *J. Phys. B: At. Mol. Phys.* **20** 1351
- [49] Hathiramani D *et al* 1996 *Phys. Rev. A* **54** 587
- [50] Bannister M *et al* 1995 *Phys. Rev. A* **52** 413
- [51] Mandelbaum P *et al* 2005 *Eur. Phys. J. D* **33** 213
- [52] Mitnik D *et al* 1996 *Phys. Rev. A* **53** 3178
- [53] Mitnik D *et al* 1997 *Phys. Rev. A* **55** 307
- [54] Lotz W 1968 *Z. Physik* **216** 241
- [55] Kelly R 1987 *J. Phys. Chem. Ref. Data* (Suppl. 1) **16**
- [56] Jordan C 1969 *Mon. Not. R. Astron. Soc.* **142** 501
- [57] Mitnik D *et al* 1994 *Phys. Rev. A* **50** 4911
- [58] Mitnik D 1996 *PhD Thesis* University of Jerusalem
- [59] Oreg J *et al* 1994 *Phys. Rev. A* **44** 1741
- [60] Fournier K B *et al* 1996 *Phys. Rev. A* **54** 3870
- [61] Carlson T *et al* 1970 *Atomic Data* **2** 63
- [62] Marr R, Elliot S and Scofield J 1997 *Phys. Rev. A* **56** 1338
- [63] Wanatabe H *et al* 2002 *J. Phys. B: At. Mol. Opt. Phys.* **35** 5095
- [64] Shi X *et al* 2005 *J. Quantum Spectrosc. Radiat. Transfer* **91** 161
- [65] Verner D and Ferland G 1996 *Astrophys. J. Suppl.* **103** 467
- [66] Nilsen J 1986 *J. Quantum Spectrosc. Radiat. Transfer* **36** 539

- [67] Nilsen J 1986 *J. Phys. B: At. Mol. Phys.* **19** 2401
- [68] Chen M 1986 *Phys. Rev. A* **33** 994
- [69] Chen M 1991 *Phys. Rev. A* **44** 4215
- [70] Roszman L 1987 *Phys. Rev. A* **35** 2122
- [71] Chen M 1988 *Phys. Rev. A* **38** 5595
- [72] Chen M 1998 *Phys. Rev. A* **58** 4539
- [73] Dasgupta A and Whitney K 1994 *At. Data Nucl. Data Tables* **58** 77
- [74] Roszman L 1987 *Phys. Rev. A* **35** 3368
- [75] Chen M 1988 *Phys. Rev. A* **38** 2332
- [76] Roszman L 1987 *Phys. Rev. A* **35** 2138
Roszman L 1989 *Phys. Rev. A* **39** 913 (erratum)
- [77] Chen M 1986 *Phys. Rev. A* **34** 1073
- [78] Hahn Y 1993 *J. Quantum Spectrosc. Radiat. Transfer* **49** 81
Hahn Y 1994 *J. Quantum Spectrosc. Radiat. Transfer* **51** 663 (erratum)
- [79] Behar E, Mandelbaum P and Schwob J L 1996 *Phys. Rev. A* **54** 3070
- [80] Behar E *et al* 1998 *Phys. Rev. A* **58** 2115
- [81] Savin D *et al* 1999 *Astrophys. J. Suppl.* **123** 687
- [82] Savin D *et al* 2003 *Astrophys. J. Suppl.* **147** 421
- [83] May M *et al* 2001 *Phys. Rev. E* **64** 036406
- [84] Mattioli M *et al* 2004 *J. Phys. B* **37** 13
- [85] Tendler M, Lackner K and Wunderlich R 1984 *Phys. Lett. A* **106** 420
- [86] Badnell N *et al* 1993 *Astrophys. J. Suppl.* **407** L91